Water vapor vertical distribution on Mars during perihelion season of MY 34 and MY 35 with ExoMarsTGO/NOMAD observations

Water vapor vertical distribution on Mars during perihelion season of MY 34 and MY 35 with ExoMars-TGO/NOMAD observations

A. Brines[1]*, M. A. López-Valverde[1], A. Stolzenbach[1], A. Modak[1], B. Funke[1], F. G. Galindo[1], S. Aoki[2,3], G. L. Villanueva[4], G. Liuzzi[4,5], I. R. Thomas[2], J. T. Erwin[6], U. Grabowski[6], F. Forget[7], J. J. Lopez-Moreno[1], J. Rodriguez-Gomez[1], F. Daerden[2], L. Trompet[2], B. Ristic[2], M. R. Patel[8], G. Bellucci[9] and A. C. Vandaele[2]

[1]Instituto de Astrofísica de Andalucía (IAA/CSIC), Spain
[2]Royal Belgian Institute for Space Aeronomy, Belgium
[3]Department of Complexity Science and Engineering, University of Tokyo, Japan
[4]NASA Goddard Space Flight Center, USA
[5]American University, Washington DC, USA
[6]Karlsruhe Institute of Technology, Institute of Meteorology and Climate Research, Karlsruhe, Germany
[7]Laboratoire de Météorologie Dynamique, IPSL, Paris, France
[8]Open University, UK
[9]Istituto di Astrofisica e Planetologia, Italy

Key Points:

- Water vapor vertical distributions during the first half of the Martian perihelion season are presented from two consecutive Martian years.
- Strong impact of the 2018 Global Dust Storm in the H_2O abundances during MY 34, showing an increase on the hygropause's altitude compared to MY 35.
- Atmospheric supersaturation events with presence of water ice at mesospheric altitudes are reported.

*Granada, Spain

Corresponding author: A. Brines, adrianbm@iaa.es

This article has been accepted for publication and undergone full peer review but has not been through the copyediting, typesetting, pagination and proofreading process, which may lead to differences between this version and the Version of Record. Please cite this article as doi: 10.1029/2022JE007273.

Abstract

The water vapor in the Martian atmosphere plays a significant role in the planet's climate, being crucial in most of the chemical and radiative transfer processes. Despite its importance, the vertical distribution of H_2O in the atmosphere has not still been characterized precisely enough. The recent ExoMars Trace Gas Orbiter (TGO) mission, with its Nadir and Occultation for MArs Discovery (NOMAD) instrument, has allowed us to measure the H_2O vertical distribution with unprecedented resolution. Recent studies of vertical profiles have shown that high dust concentration in the atmosphere, in particular during dust storms, induces an efficient transport of the H_2O to higher altitudes, from 40 km up to 80 km. We study the H_2O vertical distribution in a subset of solar occultations during the perihelion of two Martian years (MYs), including the 2018 Global Dust Storm (GDS), in order to compare the same Martian season under GDS and non-GDS conditions. We present our state-of-the-art retrieval scheme, and we apply it to a combination of two diffraction orders, which permits sounding up to about 100 km. We confirm recent findings of H_2O increasing at high altitudes during L_s = 190-205° in MY 34, reaching abundances of about 150 ppmv at 80 km in both hemispheres not found during the same period of MY 35. We found a hygropause's steep rising during the GDS from 30 up to 80 km. Furthermore, strong supersaturation events have been identified at mesospheric altitudes even in presence of water ice layers retrieved by the IAA team.

Plain Language Summary

The characterization of water vapor in the atmosphere is important for understanding the cycle of water on Mars and it is crucial in most of the atmospheric processes taking place in its current climate. The observation technique of the Nadir and Occultation for Mars Discovery onboard ExoMars Trace Gas Orbiter using solar occultations allows a high resolution vertical sampling of the atmosphere, permitting characterization of the H_2O vertical distribution. In this work we analyze the H_2O distribution in the Martian atmosphere during the southern spring in Martian years 34 and 35. A Global Dust Storm event during the first one allowed us to study the atmospheric H_2O and its response in the same season under intense and regular dusty conditions. We found that during intense dust storms, water vapor is present at higher altitudes rather than in regular atmospheric dust activity. This shows high concentrations of about 150 ppmv up to 80 km. As a consequence of the dust intensification, we observed an increase in the altitude of the 50 ppmv water vapor layer. Here we report observations

of atmospheric layers where H_2O abundances exceed the theoretical needed saturation limit even when small particles are present.

1 Introduction

The proper characterization of the vertical distribution of water vapor on Mars is a currently ongoing research field and there are many open issues in the description of the water vapor transport and distribution (Montmessin et al., 2017). Until this last decade, the water cycle has been studied with an emphasis on column densities, being the most abundant measurements available until then (Montmessin et al., 2017; Smith, 2004), and hence with a poor insight on the actual vertical distribution. Therefore, the General Circulation Models (GCMs) were the main source of information about the vertical distributions (Navarro et al., 2014). The recent possibility of systematic solar occultation observations has opened a new path towards a better understanding of the Martian climate and the water cycle. Using this technique, water vertical profiles have been studied sporadically by SPICAM onboard Mars Express (MEX). Water vapor observations have been performed also by the Mars Climate Sounder (MCS) and Compact Reconnaissance Imaging Spectrometer for Mars (CRISM) on board Mars Reconnaissance Orbiter (MRO). With SPICAM observations, previous works showed that during the dusty periods or dust storm events (e.g. 2007), the H_2O reached altitudes up to 100 km with volume mixing ratios higher than 100 ppmv (Fedorova et al., 2018), highlighting the importance of the vertical distributions for a better understanding of the physical and chemical processes driving the water cycle (Maltagliati et al., 2013). Also, researches with MCS data showed that the enhancement of water vapor and the transport of water ice by deep convection to the middle atmosphere (30-90 km) affects the hydrogen escape rate enhancing it during dust storms events (Heavens et al., 2018a). This same phenomena is also suggested by Chaffin et al. (2017, 2021) who presented results using combined data from three different spacecrafts (MRO, MAVEN and TGO).

More recent studies with the Atmospheric Chemistry Suite (ACS) on board ExoMars TGO (Fedorova et al., 2020; Holmes et al., 2021; Belyaev et al., 2021; Alday et al., 2021) revealed that the phenomenon of high altitude water vapor also took place during the Global Dust Storm in MY 34 (2018), suggesting that during dust storms, the increase of dust leads to an enhancement of the atmospheric temperatures and favors the upward transport of the water to the middle atmosphere. This same event was reported from the observations made by the Nadir and Occultation for MArs Discovery (NOMAD) instrument, also on board TGO

(Aoki et al., 2019; Villanueva et al., 2021; Neary et al., 2020).

As a result of these findings, several recent works focused in the hydrogen escape from Mars (Villanueva et al., 2021, 2022; Stone et al., 2020; Chaffin et al., 2021; Holmes et al., 2021; Alday et al., 2021) revealing the strong influence of dust storms in this process, proving the dust enhancement to have a direct effect on the escape of the hydrogen to space and suggesting that the potential for water to escape could be underestimated.

Two manuscripts related to studies of water vapor on Mars from the TGO/NOMAD data have been submitted to this issue. Aoki et al. (2022) provides an overview of the global distribution of water vapor vertical profiles from the measurements for 3.5 years, and Villanueva et al. (2022) reveals the distribution of D/H ratio in the water vapor vertical profiles near the polar regions. Also three companion papers have been submitted by the IAA/CSIC team to this special issue. All of them using NOMAD solar occultation observations, Lopez-Valverde et al. (2022) retrieves temperature and CO_2 density profiles up to 90 km from NOMAD 1st year of solar occultations, Stolzenbach et al. (2022) derives nature and composition of Martian aerosols, and Modak et al. (2022) retrieves CO vertical profiles.

Here, we present the vertical distributions of water vapor abundances retrieved from NOMAD data during the first half of the perihelion season in two consecutive Martian years (MYs). We analyze the seasonal and latitudinal variation of the water in the atmosphere, sampling an altitude range from the surface of the planet up to the mesopause at 110 km. Following Smith et al. (2017), we will refer to the altitudes below about 50 km as lower atmosphere and those above as middle atmospher or mesosphere (Lopez-Valverde et al., 2022). Also, we perform tentative characterization of the hygropause and a first estimation of the saturation ratio of the atmosphere, comparing it with water ice distribution maps. The goal of this paper is to confirm previous results on the characterization of the water abundance in the Martian atmosphere (Aoki et al., 2019, 2022; Fedorova et al., 2020; Alday et al., 2021; Belyaev et al., 2021; Villanueva et al., 2021, 2022) but also to add new insights using a wider dataset than those in (Aoki et al., 2019; Fedorova et al., 2020) incluiding observations during MY 35, processing a larger altitude range than that presented in (Aoki et al., 2022) and applying the latest instrument calibration. The analyzed period covers the Global Dust Storm (GDS) event in 2018, when large dust opacities were present in both hemispheres, in particular in the southern hemisphere (Montabone et al., 2020). This same period during MY 35 clearly showed lower dust opacities compared to MY 34 (Olsen et al., 2021) giving us the possibility of a direct comparison of the same season with different dusty

conditions: GDS and non-GDS conditions. However, after the GDS event and for the rest of the dusty season the column dust opacities in both MYs are similar (Olsen et al., 2021; Montabone et al., 2020).

This study is focused on the perihelion period from $L_s = 180°$ to $L_s = 270°$ in two consecutive Martian years, MY 34 and MY 35. The paper is structured as follows: The description of the NOMAD instrument and the dataset is presented in section 2, the analysis of the data and the methodology used are described in section 3, the description and discussion of the results are presented in section 4. Finally we present a summary and conclusions in section 5.

2 NOMAD SO measurements

2.1 NOMAD instrument

NOMAD is an infrared spectrometer covering the spectral range between 0.2 to 4.3 μm. The instrument has three spectral channels in order to observe the Martian atmosphere in nadir, limb or solar occultation geometries at different wavelengths: Two IR spectrometers, Solar Occultation channel (SO), operating in the range between 2.3 and 4.3 μm (2320-4350 cm^{-1}) and the Limb Nadir Occultation channel (LNO), operating between 2.3 and 3.8 μm (2630-4550 cm^{-1}), and a third channel operating in the UV-visible (UVIS; 200-650 nm) capable of both nadir and occultation observations (Vandaele et al., 2015, 2018)

The SO channel design is based on the Solar Occultation in the Infrared (SOIR) instrument, onboard Venus Express. It uses an echelle grating with a density of ∼4 lines/mm in a litrow configuration. An Acousto-Optical Tunable Filter (AOTF) is used to select different spectral windows (with a width that varies from 20 to 35 cm^{-1}). Each window corresponds to the desired diffraction order to be used during the atmospheric scan. The spectral resolution of the SO channel is $\lambda/\Delta\lambda \simeq 20{,}000$. The sampling time of this channel is approximately 1 second, allowing a vertical sampling of ∼1 km. Also, the AOTF permits a quick change from one diffraction order to another. As a result, the SO channel is able to probe the atmosphere at a given altitude through 6 different diffraction orders quasi-simultaneously (within 1 second).

2.2 Dataset selected for this work

NOMAD science operations began in April 2018 and up to this date, almost daily observations have been performed since the middle of MY 34 (Mar 2018-Mar 2019). For this study, we have selected two subsets of measurements taken by the NOMAD SO channel covering the same Solar Longitud period L_s =180-270° in two different Martian years: MY 34 (during the period from 22 May to 8 October 2018) and MY 35 (during the period from 18 April to 29 August 2020). Water vapor spectral absorption lines are present over a wide range of the IR spectrum. Since CO_2 is the dominant gas in the Martian atmosphere, we have to select a spectral range free of CO_2 lines in order to be able to detect the H_2O lines. For that reason we have decided to analyze observations taken at the NOMAD SO diffraction order 134 (3011-3035 cm^{-1}) and order 168 (3775-3805 cm^{-1}). Order 134 has absorption H_2O lines with a moderate intensity ($I \sim 10^{-21}$ $cm^{-1}/(molecule \cdot cm^{-2})$) allowing the study of the lower atmosphere where lines are not heavily spectrally saturated (Aoki et al., 2022), while order 168 has stronger lines ($I \sim 10^{-19}$ $cm^{-1}/(molecule \cdot cm^{-2})$) allowing the sounding at higher altitudes. By spectral saturation we refer to how the absorption lines penetrate into the continuum of the spectrum. In optically thin conditions, the line depth increases proportionally with the gas density. When in saturated conditions, the line core stops growing and the overall absorption does not follow the gas density anymore. As a consequence of this limitation, each order has an optimal altitude range to be used: order 134 for the lower atmosphere and order 168 for the upper atmosphere. The data set has been selected including simultaneous observation of both diffraction orders. With this two subsets, a total of 962 occultations have been analyzed, including observations in both hemispheres at different latitudes. Latitudinal coverage over solar longitude of the occultations is shown in Figure 1, also indicating the Local Solar Time of the observations, each point representing one single occultation.

3 Data analysis

3.1 Data cleaning and pre-processing

In this work we used Level 1 SO data (i.e. calibrated transmittances) from the NOMAD SO channel. Although a lot of effort has been devoted to their spectral calibration (Thomas et al., 2021; Trompet et al., 2022; Villanueva et al., 2022), there are still some inaccuracies which can affect the performance and quality of the retrievals. The most relevant to take

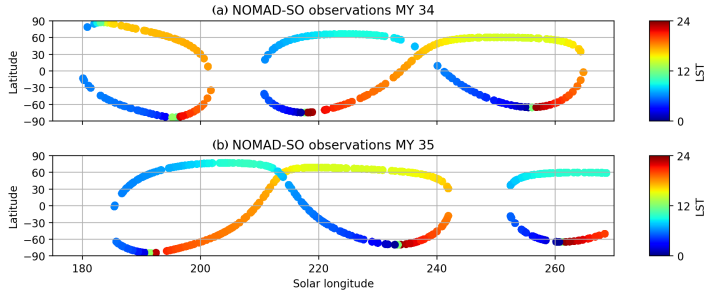

Figure 1. Latitude of the analyzed NOMAD SO observations over solar longitude for: (a) MY 34 and (b) MY 35. Color indicates local solar time of the measurements.

into account are: the spectral calibration uncertainty, a residual bending in the spectral dimension and the effects of the AOTF and the instrumental line shape (ILS). Last two affecting the forward model calculation are described in section 3.2.2. At IAA we have developed pre-processing tools to identify and eliminate the residual bending and to do a first estimation and correction of the spectral shift using the line-by-line radiative transfer algorithm KOPRA (Karlsruhe Optimized and Precise Radiative transfer Algorithm) (Stiller, 2000) developed at IAA and IMK (Institut für Meteoriologie und Klimaforschung) in Karlsruhe, Germany. The pre-processing is described in some detail in a companion paper in this special issue (Lopez-Valverde et al., 2022), but a summary is included. It proceeds in several steps, separating different components of the measured transmittance. Also the pre-processing computes the aerosol slant optical depth, which is used later to retrieve extinctions at the tangent point (Stolzenbach et al., 2022). These values are used during gas retrievals, like H_2O, CO_2 (Lopez-Valverde et al., 2022) or CO (Modak et al., 2022) following a sequential retrieval chain. This pre-processing works considering the measured transmittances (T) corrected for spectral shift ($\Delta\lambda$) as a proportional combination of the forward model (T_0) scaled by a factor (k), the residual bending (T_b) and the aerosol slant opacity (τ). These transmittances are combined with the instrumental response in a precise line-by-line calculation using the KOPRA forward model. One of the possible ways to express the measured transmittance is the following one, which is useful to correct for the spectral bending:

$$T(\lambda + \Delta\lambda) = T_0^k(\lambda)\ T_b(\lambda)\ \mathrm{e}^{-\tau} \tag{1}$$

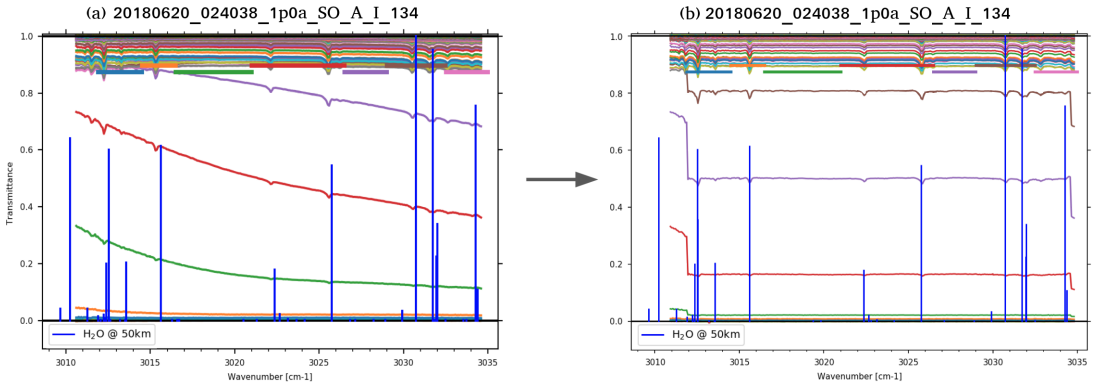

Figure 2. Examples of NOMAD SO transmittances from diffraction order 134 before the cleaning process (a) and after the first correction of the spectral shift and the bending (b). Each color indicates a different tangent altitude (left and right panel do not share the same color scheme). The vertical blue lines indicate the positions of the H_2O absorption lines from HITRAN 2016 and their relative line intensity to a normalization of the strongest line in the measured spectral range.

Then, using an optimized brute force method, we compute an extensive set of simulated spectra for each measured spectrum using a radiative transfer line-by-line calculation. In principle, this set of simulations shall cover a large grid of the three cleaning parameters (scale factor, bending and aerosol slant opacity), however, we have implemented a jump search algorithm in order to reduce the number of simulations speeding up the convergence. The goal is to select the optimal combination of parameters , i.e., that which gives the lowest variance when compared to the data. Afterwards, by adjusting the position of the CO_2 and H_2O absorption lines to the position from HITRAN 2016 database (Gordon et al., 2017), we perform a first correction of the spectral shift. Figure 2 shows an example of the cleaning process applied to order 134. Left panel shows the spectra before cleaning, where large bending can be observed at some altitudes. This bending is caused by the instrument and is larger than the expected bending due to water ice scattering. Right panel in Figure 2 shows the spectra after the cleaning process, where the different baseline levels observed are due to aerosol attenuation. We have excluded the edges of the spectra from any cleaning and inversion process due the large level of noise in those regions. Based on the estimated aerosol opacity, we apply a cloud filter to the data excluding the observations close to the surface where the slant opacity estimated to be greater than 2.0 and selecting the minimum altitude where the gradient in the slant opacity is smaller than 0.08 km^{-1}.

3.2 Retrieval scheme

3.2.1 A priori climatology

The *a priori* temperature and density profiles needed by the forward model are obtained in this work from the Mars Planetary Climate Model developed at the Laboratoire de Météorologie Dynamique (LMD Mars PCM) (Forget et al., 1999), using the latest implementations of the dust and water cycles described in Navarro et al. (2014) and a new comprehensive photochemical scheme (Lefèvre et al., 2021) covering all atmospheric layers from the surface to the exobase. Simulations with the dust scenarios appropriate for MY 34 and MY 35 (Montabone et al., 2015, 2020) were conducted. For each observational profile, we extract the modeling results interpolating at the exact location (latitude, longitude) and time (L_s, local time) of the observation, provided by the navigated NOMAD data at 50 km altitude. Ideally, when the signal is sufficient, the retrieval results are basically independent of the a priori. Hence, using a climatological model is appropriate for creating this a priori climatology.

3.2.2 Forward model

For both the cleaning of the data and the water vapor inversions, we simulate the spectra with KOPRA. As a line-by-line and layer-by-layer code, KOPRA was designed to calculate the infra-red radiative transfer through the atmosphere. An extensive description of this line-by-line radiative transger algorithm can be found in (Stiller, 2000). Originally developed for the Earth, KOPRA was recently adapted to limb emissions on Mars (Jiménez-Monferrer et al., 2021) and for this work it has been adapted to solar occultation data on Mars for the first time. Some modifications have been made in order to make the code suitable for the analysis of the NOMAD data. Because of the AOTF, the NOMAD SO spectra of a certain diffraction order also includes the signal from several adjacent orders. That is, the data to be analyzed is a combination of several diffraction orders (Neefs et al., 2015). Therefore, understanding and characterizing the AOTF and ILS is mandatory to accurately simulate the instrumental effects in the measured data. A first attempt to characterize these instrumental effects was performed during in-flight calibrations, summarized in (Liuzzi et al., 2019; Thomas et al., 2021). More recently, a revision by several teams within the NOMAD consortium improved the AOTF and ILS descriptions (Villanueva et al., 2022; Lopez-Valverde et al., 2022). It was found that the AOTF transfer function can be described

with an asymmetric Sinc function added to a Gaussian offset. The parameters that describe the AOTF are order dependent. Also, as shown in Thomas et al. (2021) it was found that the ILS can be described by two Gaussian functions with a separation and a scaling ratio between them that varies across the diffraction orders. A large amount of effort has been devoted in the last year within the NOMAD consortium to identify the key parameters and to characterize those variations with a proper parameterization. This is described in detail in Villanueva et al. (2022). In this work we have adopted the nominal parameters for the ILS and AOTF parameterization proposed by Villanueva et al. (2022). The new AOTF and ILS significantly improved the convergence of the fittings in our H_2O retrievals and the agreement between different diffraction orders.

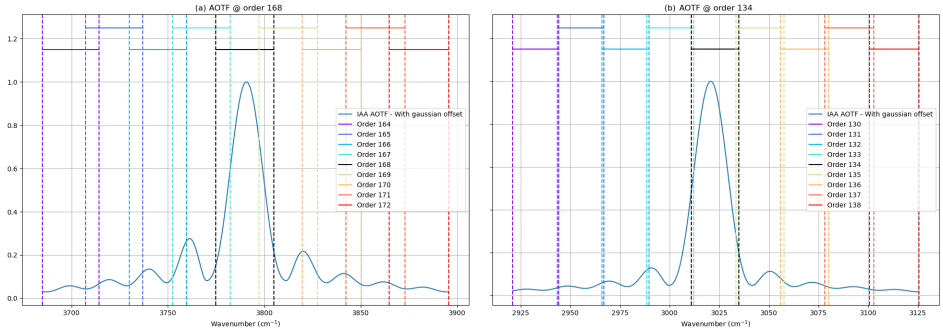

Figure 3. NOMAD SO AOTF functional for orders 134 (a) and 168 (b). Vertical dashed lines indicate the limits of the diffraction orders. Only +/- 4 adjacent orders are represented.

In Figure 3 we show the AOTF normalized functionals used for orders 134 and 168. For the analyzed diffraction orders, the simulated spectra is calculated taken into account the flux contribution of +/- 4 adjacent orders (i.e. orders 164 to 172 for the order 168 and orders 129 to 138 for the order 134) since the contributions of further orders starts to be less relevant as the number of adjacent order increases. In Figure 4a we show reference KOPRA radiances for order 168 calculated considering 0, 1, 3 and 4 adjacent orders (for example, the radiance calculated considering 4 adjacent orders has been obtained taking into account orders 164, 165,..., 168,...,171, and 172).In Figure 3, colors denote NOMAD orders while in Figure 4, they indicate the number of adjacent orders included during the radiance simulations. Panel 4b shows the relative difference between each radiance referred to the radiance computed with 4 adjacent orders, highlighting the main contribution comes the first +/- 1 adjacent orders and no more than a 5% contribution comes from the +/- 3rd

adjacent orders. Also, increasing the number of adjacent orders has a direct impact in the calculation time of the forward model, so a balance between performance optimization and accuracy has to be taken into account.

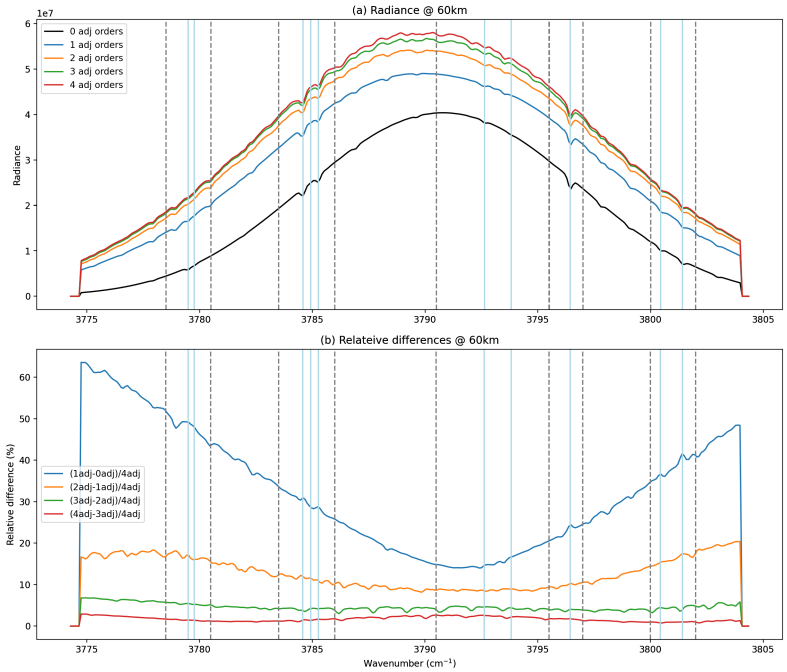

Figure 4. Examples of radiances computed with KOPRA for the order 168 considering a different number of adjacent orders. Panel (a) shows the radiances calculated with 0, +/- 1 (167-169), +/- 2 (166-170) , +/- 3 (165-171) and +/- 4 (164-172) adjacent orders. Panel (b) shows the relative differences between them refereed to the radiance calculated with 4 adjacent orders, where the relative individual contribution of the adjacent orders can be seen. Vertical solid lines indicate the positions of the strongest H_2O absorption lines. Vertical dashed lines indicate the limits of the micro-windows used for the retrievals

An example demonstrating the NOMAD-specific KOPRA forward modeling applied to a monochromatic transmittance spectrum is summarized in Figure 5. First, the monochromatic spectrum (a) is convolved with the ILS (b). Then, the AOTF filter is applied (c) and the contributions from adjecent orders are shifted to the central order and added (d) to generate the final spectrum to use during the retrievals (e).

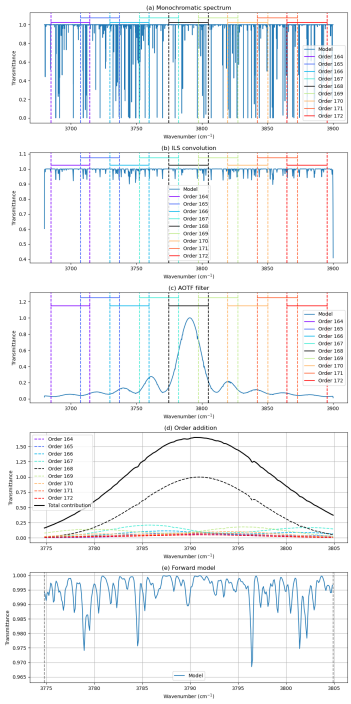

Figure 5. Example of the NOMAD-specific forward modeling steps applied to a monochromatic spectrum (a): ILS convolution (b), AOTF transfer function application (c), adjacent orders addition (d) and final spectrum used for the retrieval (e). Panels (d) and (e) cover a smaller spectral range than panels (a)-(c).

3.2.3 Inversion and convergence criteria

For the H_2O inversion we use the Retrieval Control Program (RCP) developed at IMK, which incorporates the KOPRA forward model. After providing an *a priori*, a first-guess and the measured spectra, RCP solves the inversion problem iteratively until the convergence of the solution. The IMK-IAA level-2 processor relies on multi-parameter non-linear least squares fitting of measured and modeled spectra (von Clarmann et al., 2003). Further information about RCP and the inversion problem can be found in (Jurado Navarro et al., 2016). We use a first order Tikhonov-type regularization optimized for each diffraction order. Also we apply a strong diagonal constrain at the lowermost altitudes (below 1 km) and at high altitudes where no information form the spectra is expected (above 95 km in order 134 and above 110 km in order 168). For this study, we are considering the measurement errors in the data provided by Thomas et al. (2021) as pure uncorrelated random errors, giving as a

result a diagonal measurement noise covariance matrix whose elements are defined as:

$$S_{ij} = \langle (\epsilon_i - \langle \epsilon_i \rangle)(\epsilon_k - \langle \epsilon_j \rangle) \rangle \ , \tag{2}$$

where $S_{ij} = 0$ when $i \neq j$.

After the convergence of the retrieval, RCP generates the vertical profiles of the targeted species, the noise error covariance matrix in the retrieval parameter domain, the averaging kernels and the vertical resolution. A sample of those products obtained for orders 134 and 168 are shown in Figure 6.

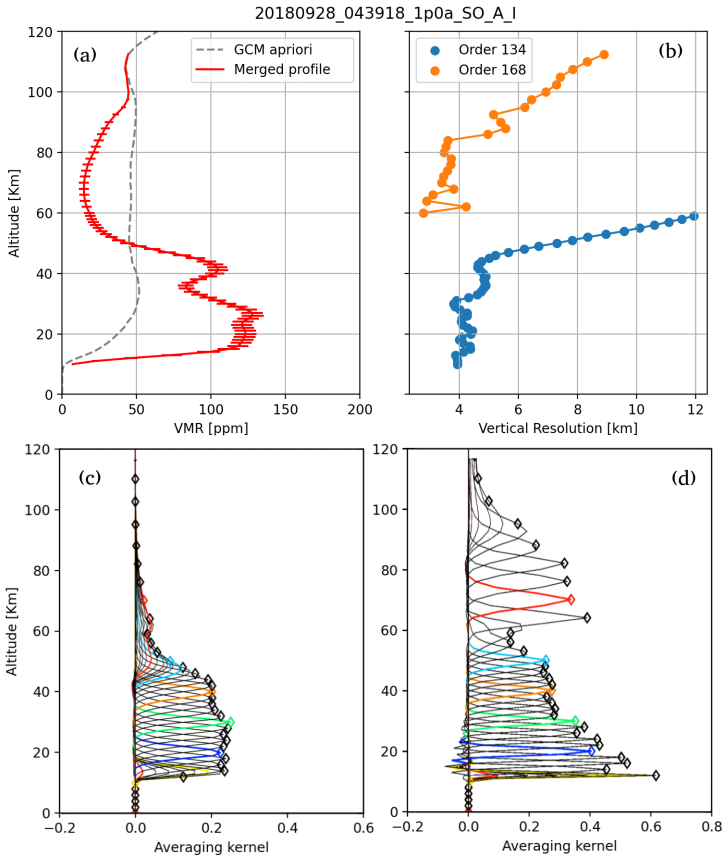

Figure 6. Performance of the retrieval of the data taken at the observation 20180928_043918_1p0a_SO_A_I. Panel (a) shows the retrieved water vapor, panel (b) shows the vertical resolution obtained for the order 134 (blue) and 168 (orange). Bottom panels show the the averaging kernels of the retrievals for orders 134 (c) and 168 (d)

Previous to the analysis of the dataset presented here, we have performed several tests with synthetic spectra mimicking the NOMAD SO instrument (AOTF, ILS and instrumental random noise) and the Martian atmosphere (realistic aerosol vertical distribution profiles) in order to prove the stability and performance of our cleaning and retrieval setup. Also, in order to check for the independence of the retrieved profiles to the used climatology we have performed synthetic retrievals modifying the *a priori* and first-guess inputs like H_2O VMR or temperature. Regarding this last one, and in contrast to other retrieval targets that our team has also delivered (temperature, CO abundances), the assumed temperature is of minor importance for H_2O.

Discrete spectral ranges (i.e. Micro-Windows; MWs) can be selected in order to optimize the retrieval. For each diffraction order we have selected different MWs corresponding to those regions where strong absorption lines are present. Here we differentiate two sets of micro-windows: Cleaning-MWs and Retrieval-MWs. MWs selected for this work are described in Tables 1 and 2. The first set corresponds to the spectral ranges used during the cleaning process and cover almost the full order (just excluding the edges). The second set, included in first one, corresponds to those MWs used for the retrieval, and only those with strong absorption lines are considered.

Table 1. Micro-windows (cm^{-1}) used for the orders 134 during the cleaning and the retrieval process. (∗) denotes MWs used for the retrieval.

Order	MW1	MW2*	MW3	MW4*	MW5	MW6*	MW7	MW8*	MW9
	3012.9	3014.8	3016.5	3021.5	3023.0	3024.8	3026.5	3029.8	3032.5
134	|	|	|	|	|	|	|	|	|
	3014.8	3016.5	3021.5	3023.0	3024.8	3026.5	3029.8	3032.5	3034.0

To obtain the water vapor vertical profiles, we follow a sequential retrieval scheme. First we retrieve a spectral shift correction from the cleaned data within a confined altitude range of just 10-20 km where the absorption lines are clearly visible. In order to have a proper characterization and stability, water vapor also is retrieved but the result is not considered in this first stage. After that, we retrieve the water vapor vertical profile in the full altitude range for each order (except the lowermost altitude range excluded by the cloud

Table 2. Micro-windows (cm^{-1}) used for the orders 168 during the cleaning and the retrieval process. (∗) denotes MWs used for the retrieval.

Order	MW1	MW2*	MW3	MW4*	MW5	MW6*	MW7*	MW8	MW9*	MW10
	3777.0	3778.5	3780.5	3783.5	3786.0	3790.5	3795.5	3797.0	3800.0	3802.0
168	|	|	|	|	|	|	|	|	|	|
	3778.5	3780.5	3783.5	3786.0	3790.5	3795.5	3797.0	3800.0	3802.0	3803.0

filtering). Along with the water vapor, a spectrally constant transmittance level is adjusted to account for the impact continuum absorption by aerosols. A full aerosol optical depth retrieval is done by Stolzenbach et al. (2022) and its results about the water ice particles characterization are used in this work. Finally, when orders 134 and 168 are measured during the same atmospheric scan, we merge both profiles using the result from order 134 for the lower atmosphere and the result from order 168 for the upper atmosphere.

3.2.4 Merging of diffraction orders 134 and 168

The performance and confidence on the retrievals from orders 134 and 168 can be obtained after a statistically large number of occultations. Below about 60 km, the order 168 usually shows an unstable behavior, being deeply sensitive to the AOTF characterization due to the presence of spectrally saturated lines, while order 134 has a good response in this altitude range, with a good retrieval performance, i.e, small residuals as shown in Figure 7 (bottom panels). Above 60 km, the absorption lines in order 134 begin to be very noisy, while those observed with the order 168 begin to be optically thin. This feature can also be observed in Figure 7 (top panels) where the residuals of the order 168 are better in this altitude range and the spectra observed with order 134 becomes too noisy with no visible absorption lines. For this reason, as a general criterium we decide to use the order 134 to probe the atmosphere below 60 km and order 168 above where optically thin lines above noise are present in both orders. The value of 60 km has been assumed for simplicity, small changes in this transition altitude have little impact on our results. In some particular occultations where only observations from order 134 are available, a vertical extension of this criterium is applied to those altitudes where the retrieved averaging kernels (AvK) are larger than 0.03 (below that value we consider that the information in the retrieved profile mainly comes from the a priori climatology), allowing us to retrieve information up to 80-90 km. After

some experimentation, we set this minimum value at 0.03; small changes around this value do not alter the results. There are other scans where the sensitivity in the order 134 drops at altitudes lower than 60 km, as shown by the AvK diagonals being lower than 0.03. In these cases, we maintain the general rule mentioned above for order 168, of considering only retrieved H_2O abundances above 60 km. Therefore, in these cases there is a gap between the upper altitude sounded in order 134 and that in order 168, where our retrieval results basically supply the climatological a priori H_2O. In the figures that follow in sections 4.1 and 4.2, we do not show those a priori values but focus on the purely NOMAD retrievals, i.e., instead of adding the a priori values to form a full profile we decide to leave an altitude gap between the two NOMAD orders to highlight the altitudes actually sounded. Regarding the merging, first the retrieval using the order 134 is done for the full altitude altitude range, although the sensitivity to what happens above 90 km is very limited due to the noise in the measurements of this order. Then, we perform the retrieval of the order 168 for the full altitude range too, but using the retrieved H_2O from order 134 as a priori instead of using the PCM climatology and applying a strong diagonal constrain in the the altitude range below 60 km with a smooth transition to a non-diagonalized region above that altitude. As a result, we obtain a profile merging information from order 134 below 60 km and from order 168 above. Note that we do not combine the two profiles by weighting them. We think that a combination of these two full profiles is risky and prone to errors due to the very different optical thickness between orders 134 and 168 and to any possible incompleteness in handling the error propagation in each of them. In Figure 8 we present an example of the order merging in two different occultations. Note that the difference between the combined profile and both 134 and 168 around 65 km is due to the global fit used, which tries to find the best match at all altitudes, although this effect is within error bars.

3.3 Comparison and validation

Vertical profiles of H_2O abundance from the NOMAD SO channel have been previously presented in a couple of papers (Aoki et al., 2019; Villanueva et al., 2021) and also in a companion paper in this issue (Aoki et al., 2022). In Aoki et al. (2022) (A22) a comparison with ACS near-Infrared channel (NIR) retrievals (Fedorova et al., 2020) is performed,revealing that ACS H_2O abundances are 22% higher than their results. An important difference is that the ACS retrievals used measured temperatures in each scan by the same instrument, while A22 and co-workers used modeled temperatures. However, this result improves those

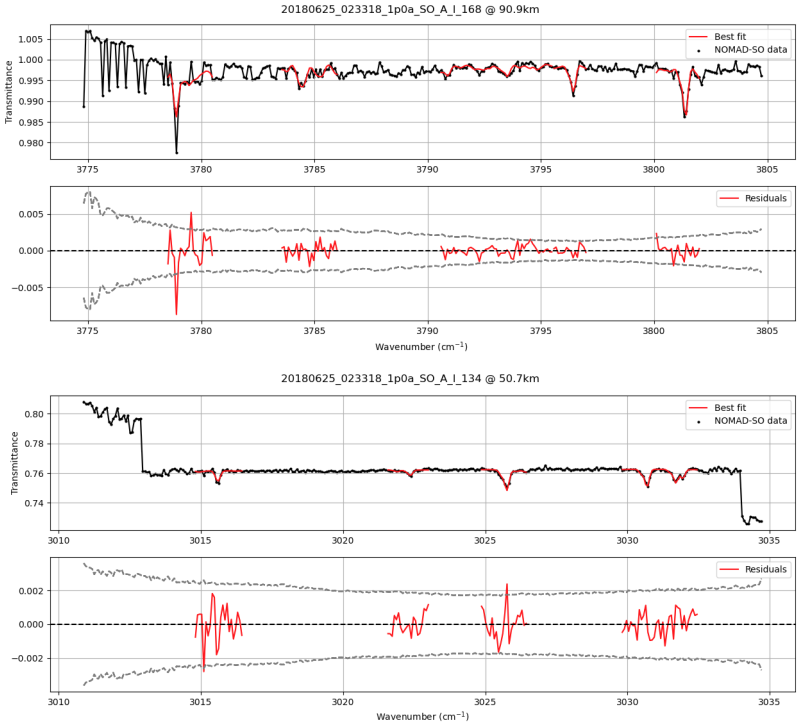

Figure 7. Example of the best fit and the residuals obtained after the retrieval. Two top panels show the data from order 168 at 90 km and two bottom panels the data from order 134 at 50 km.

presented in Aoki et al. (2019) (before the improvements in the AOTF/ILS characterization), where water vapor abundances were much higher than those in Fedorova et al. (2020). We have performed a first comparison with A22 for validation purposes, using data from diffraction order 134. Some caution is needed before comparing VMR, as this is a ratio of the H_2O abundance to the total abundance, and each team used a different reference PCM, and thus the atmospheric densities are not necessarily similar. To eliminate this effect, the A22 profiles have to be corrected scaling the VMR by a density factor at all altitudes. We present the global comparison of the scaled results in Figure 9, showing a qualitative agreement between both retrievals. The linear weighted fitting of the data suggests that our retrievals are systematically higher than A22 by about 13%. In Figure 10 we present a direct comparison of eight individual vertical profiles from A22 with our retrievals. We observe a good agreement between most of the profiles (profiles with large discrepancy have been selected on purpose to highlight the necessity of a proper comparison work), despite using different methodologies with very different approaches. However, there are some discrepancies beyond the uncertainty range in some profiles, in particular in the altitude range

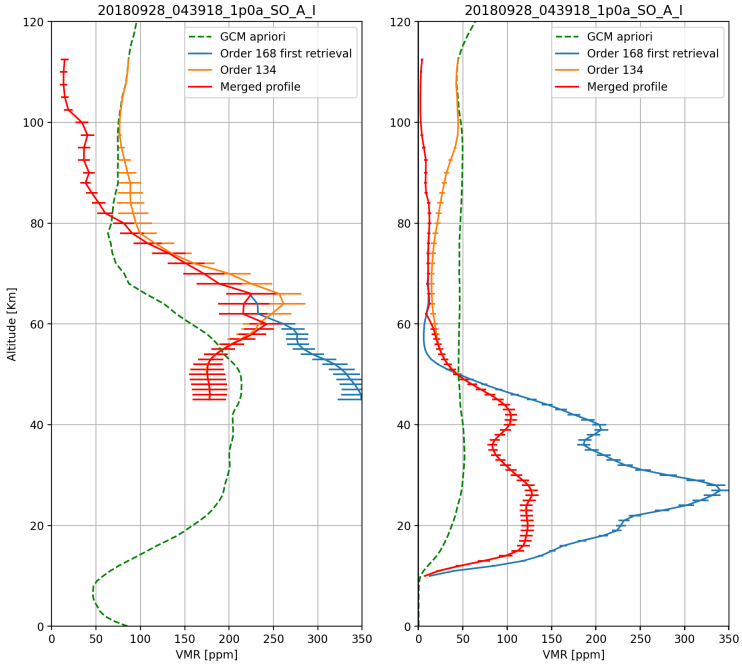

Figure 8. Two examples of the merging of vertical profiles from orders 134 and 168. Note that the merged profiles (red) overlaps the 134 order (orange) below 60 km whereas it overlaps the 168 order (blue) above.

between 10-20 km where no scientific conclusions have been drawn due the difficulty of obtaining results caused by the large dust opacity. The origin of this differences and its implication will be further investigated in future works with a proper and more detailed comparison that is beyond the scope of this work.

Also a discussion on the global H_2O distribution has been held in Section 4 of this work with the results by Aoki et al. (2019, 2022) using NOMAD data, and by Fedorova et al. (2020) and Belyaev et al. (2021) and Alday et al. (2021) with ACS data, showing that the seasonal variation maps along with the latitudinal maps and the saturation ratio maps that we present here reveal similar structures and features as those previously presented.

4 Results and discussion

Water vapor vertical profiles obtained after the inversion process allow us to generate different sub-products and study different aspects of the Martian atmosphere. Here we present detailed vertical distribution maps of the same seasonal period in two different MYs. The data analyzed covers a solar longitude range of 90°, form $L_s \sim 180°$ to

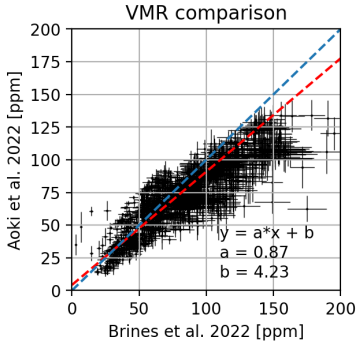

Figure 9. Comparison of the water vapor volume mixing ratio retrieved by Brines et al. (2022a) and Aoki et al. (2022). The blue dashed line shows the curve $y = x$ and the red dashed line represents the linear weighted fitting of the scattered data.

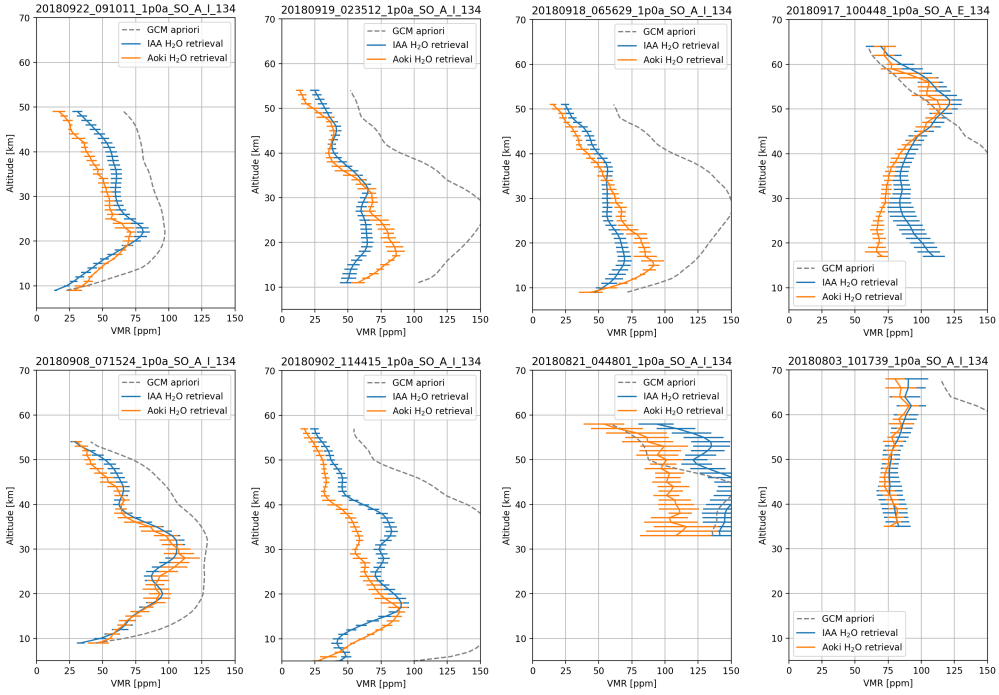

Figure 10. Examples of eight water vapor vertical profiles retrieved by Brines et al. (2022a) (blue) and Aoki et al. (2022) (orange) using observations from diffraction order 134. Gray dashed line shows the Mars PCM *a priori* used for Brines et al. (2022a) retrievals.

$L_s \sim 270°$. This selected range allow us to study the water vapor distribution during the same season with and without the MY 34's GDS.

4.1 Martian Year 34

4.1.1 Seasonal variation

The growth and maturation phase of the 2018 Global Dust Storm took place during the period covering a solar longitude range from $L_s \sim 190°$ to $L_s \sim 210°$ and with a long decay phase that extended until $L_s \sim 270°$ (Kass et al., 2020; Guzewich et al., 2019). This period corresponds with the northern autumn (southern spring) in Mars, which spans from $L_s = 180°$ to $L_s = 270°$. During this period, following the global seasonal trend as it was understood prior to 2018 observations, the northern hemisphere gradually starts to be colder at high latitudes as the northern autumn progresses (Smith et al., 2017). After $L_s = 170°$, water vapor abundances decrease in the north polar regions followed by an increase moving southwards and reaching a maximum between 30°N and the equator that remains during the whole northern winter (Montmessin et al., 2017). In the southern hemisphere, water vapor progressively increases due to the southward transport and the temperature increase, leading to the southern polar cap sublimation at late southern spring(Montmessin et al., 2017). Southern spring and summer are warmer and wetter than the analog northern seasons, in particular at mid-low latitudes. The reason for this behavior is that the southern summer coincides with the perihelion of the Martian orbit so the radiation influencing the planet increases, and compared with the northern summer, the southern summer is noticeable warmer (Smith et al., 2017), and more water vapor from water ice sources can sublimate and ascend to the atmosphere (Montmessin et al., 2017). This classical description is under revision by recent detailed views of the vertical structure of temperature and water vapor that TGO instruments are providing (Fedorova et al., 2020; Belyaev et al., 2021; Lopez-Valverde et al., 2022; Aoki et al., 2019, 2022; Villanueva et al., 2021), showing a distinct warming and moistening of the atmosphere in both hemispheres by $L_s \sim 200°$. During the GDS in MY 34, due to the huge amounts of dust, the atmosphere temperature in both hemispheres increased as a consequence of the absorption of the solar radiation by the dust particles (Neary et al., 2020; Montabone et al., 2020).

The seasonal variation maps are presented in Figure 11 for the northern (left panels) and southern (right panels) for MY 34. We present in Figure 12 a detailed insight of the water vapor in the upper atmosphere in order to highlight features below 100 ppmv. For the representation of both Figures, we have filtered the profiles to those altitudes where

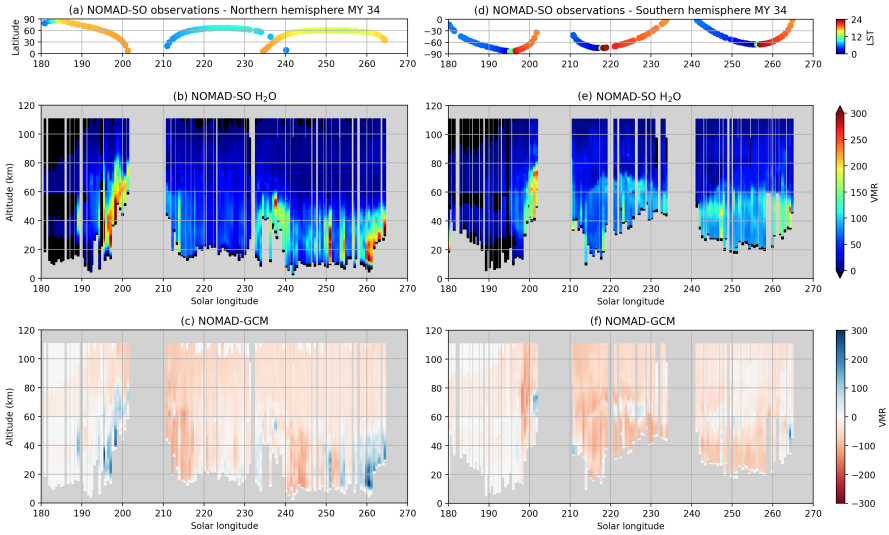

Figure 11. Seasonal vertical distribution maps of the retrieved water vapor (b,e) and the differences between the NOMAD SO retrievals and the PCM climatology (c,f) during the MY 34 in the Northern (left panels) and the Southern (right panels) hemispheres. Top panels (a,d) show the latitudes and the Local Solar Time of the observations analyzed. Black regions in panels (b) and (f) are masked due to the low averaging kernels obtained during the retrievals.

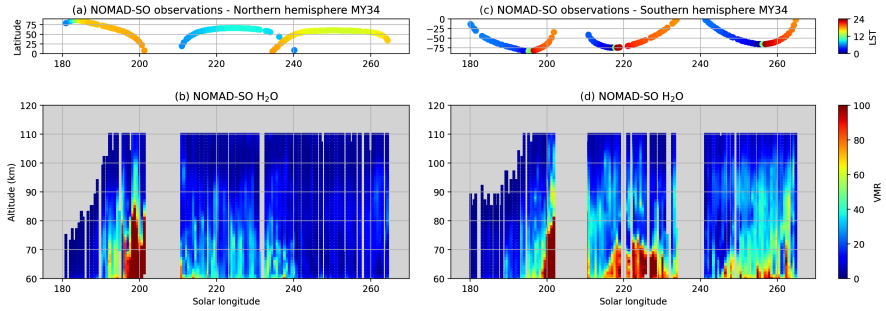

Figure 12. Seasonal vertical distribution maps of the retrieved water vapor at the upper atmosphere above 60 km during the MY 34 in the Northern (b) and the Southern (d) hemispheres. Top panels (a,c) show the latitudes and the Local Solar Time of the observations analyzed.

the averaging kernels of the retrievals are larger than 0.03 in order to exclude those regions where there is not enough information in the spectra to retrieve water vapor and hence, the profile would be purely mimicking PCM climatology. Those low information regions have been colored black. As shown in Figure 11, during the mature of the GDS we observe an intense peak in the water vapor volume mixing ratio, showing water abundances of ∼150 ppmv at 80 km and ∼30 ppmv up to 100 km in both hemispheres followed by a decrease of

the water abundances to ∼50 ppmv below 60 km just after the strong activity of the storm at $L_s \sim 210°$, shown in Figure 12. A possible explanation for this phenomenon is that due to the increased temperatures as a consequence of the dust enhancement, water vapor is not able to condense into ice as it ascends in the atmosphere, preventing the sedimentation of ice particles and due to the enhanced global circulation, allowing the water vapor to reach high altitudes (Neary et al., 2020). This increase is thought to be due to the intensification of the upward branch of the Hadley cell (Heavens et al., 2018b; Fedorova et al., 2020). This same feature is presented in Belyaev et al. (2021), observing water vapor abundances about 10-30 ppmv at 100 km during the perihelion of MYs 34 and 35. We also observe a peak in the water vapor VMR in the northern hemisphere at $L_s \sim 235°$ corresponding to observations at low-mid latitudes and near the equator where higher temperatures and hence higher amounts of water vapor are expected. In this case, the water vapor is mostly confined within an altitude range between 30-60 km. In the southern hemisphere, we observe a progressive increase in the water vapor abundances at $L_s > 220°$, with a clear propagation up to 100 km of water vapor abundances larger than 40 ppmv as can be seen in Figure 12. This occurs because at this period of time, deep into the southern spring, the temperature increases gradually and the sublimation of the southern polar cap releases huge amounts of water vapor into the atmosphere. Then, due to the Hadley circulation intensification during this season and the eddy diffusion, water vapor can be distributed to lower latitudes (Smith, 2002). The intensification of the Hadley cell during the perihelion of MY 34 is directly observed by Olsen et al. (2021), suggested to be the reason for the rapid increase in the observed CO VMR above 80 km instead of the 60 km predicted by the PCM. Our H_2O distribution has many similarities with previous results from recent TGO publications (Fedorova et al., 2020; Aoki et al., 2019, 2022; Villanueva et al., 2021; Belyaev et al., 2021; Alday et al., 2021). Focusing on the works by Fedorova et al. (2020) who measured atmospheric temperatures using ACS NIR and by Aoki et al. (2019, 2022) using NOMAD SO, which are cited as F2020 and A2022 hereafter, we confirm the following five features: (a) Both F2020 and A2022 also found a water vapor peak at 80 km/in the lower mesosphere during the mature phase of the GDS ($L_s = 195 - 205°$) (b) both works also reported the decline in VMR after $L_s \sim 210°$ (c) the peak at $L_s \sim 235°$ in the northern hemisphere that we reported was also observed by both works and discussed by A2022. (d) significant water vapor abundances up to 100 km around $L_s \sim 260°$ in the southern hemisphere were also reported by F2020, but not by A2022 due to its limitation in altitude coverage. (e) the lowermost altitude of the H_2O profiles varies

with latitude and season, as it is very dependent on the amount of aerosols in the lower atmosphere, and this variation is entirely similar to F2020 and A2022, although perhaps we are using a slightly more conservative criterion (our lowermost retrieved altitudes are a little bit higher). We also observe a few quantitative differences with those works, like these two main features : (a) F2020 shows overall larger water vapor abundances above 60 km in the southern hemisphere than those presented in this work at $L_s = 210 - 220°$ and $L_s = 250 - 260°$. This discrepancy is also found at $L_s = 210°$ in the northern hemisphere in A2022 too. (b) Comparing with Villanueva et al. (2021) we observe a discrepancy at $L_s = 240°$ in the northern hemisphere, showing water vapor abundances about 10-20 ppmv larger in this work than in Villanueva et al. (2021).

4.1.2 Hygropause

On Earth, the region of the atmosphere near the tropopause where the water vapor reaches its minimum value is called the hygropause and can be found at ∼20 km (Kley et al., 1979). On Mars, the absence of stratosphere and the vertical variability of the water vapor makes it difficult to fix an altitude for the hygropause. Different definitions of this atmospheric layer can be found in several works (a cold layer at 40-50 km altitude at which H_2O condenses, (Stone et al., 2020); the altitude where the water vapor volume mixing ratio drops below 70 ppmv, (Holmes et al., 2021) or where water content rapidly decreases to effectively zero, (Heavens et al., 2018b)). For this work we use a simple definition for this layer: the altitude where the water vapor volume mixing ratio starts to be lower than 50 ppmv.

Figure 13 shows the altitude level of the hygropause (as defined above in this section). We observe a clear increase in both hemispheres at $L_s \sim 200°$ as a result of the water vapor injection due to the GDS (Aoki et al., 2019; Chaffin et al., 2017; Fedorova et al., 2020; Belyaev et al., 2021). Fedorova et al. (2020) found comparable hygropause altitudes in both hemispheres and we confirm this result, although we find that after the intense activity of the dust storm, overall the hygropause level in the northern hemisphere with a mean altitude about 50 km, is lower compared to the southern hygropause observed at 60-70 km. This is expected since northern autumn is drier at lower altitudes near the troposphere according to (Smith, 2002, 2004). This rising of the southern hygropuse also being noticeable at mid-low northern latitudes is due to the expansion of the lower atmosphere caused by the temperature increase. Also in the southern hemisphere, we observe peaks in the hygropause

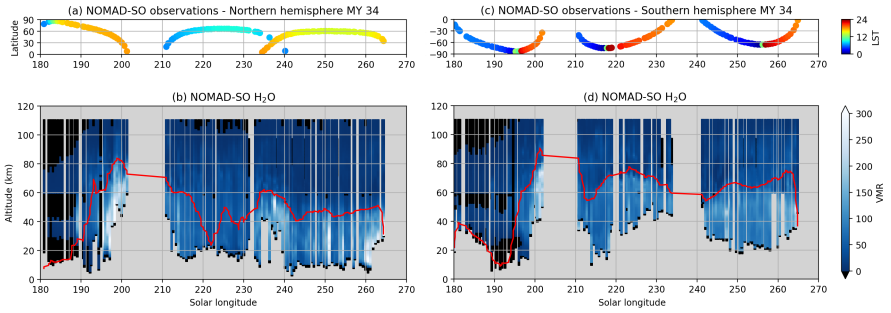

Figure 13. Seasonal vertical distribution maps of the retrieved water vapor (b,d) during the MY 34 in the Northern (left panels) and the Southern (right panels) hemispheres. The red line indicates the hygropause level. Top panels (a,c) show the latitudes and the Local Solar Time of the observations analyzed.

level at $L_s \sim 220°$ and $L_s \sim 260°$ corresponding to observations at ~60-50°S. We attribute these peaks to two factors: (a) an enhancement of water vapor occurs due to the Hadley cell circulation, whose upwelling branch moves to mid southern latitudes during this period rising water vapor and transporting it northwards across the equator (Steele et al., 2014) and (b) an increase of the temperatures at 50-60 km observed by Lopez-Valverde et al. (2022) preventing water vapor from condensing.

4.1.3 Latitudinal variation

In Figure 14 we show the latitudinal variation of the water vapor for the analyzed period of the MY 34. Panel 14a shows the period just before the GDS. We observe a dry atmosphere in both hemispheres with small amounts of water vapor about ~50 ppmv for the southern hemisphere and ~100 ppmv present at very high latitudes. In panel 14b, during the period of strong activity of the GDS we observe a clear increase of the water vapor VMR with the water confined mostly between 60°N and 75°S and reaching altitudes up to 80 km at mid latitudes with abundances about 150 ppmv. After the peak of the GDS, the amount of H_2O in the atmosphere reduces again as shown in 14c. Panels 14d and 14e correspond to the seasonal period deep into the southern spring during L_s = 220-260°. Here we observe the effects on the progressive increase of the upper atmosphere temperature, allowing more water vapor be present in the atmosphere. Also more water is progressively available in the atmosphere due to sublimation of the southern polar cap (Villanueva et al., 2022). We also observe high amounts of water vapor at northern mid latitudes extending up to

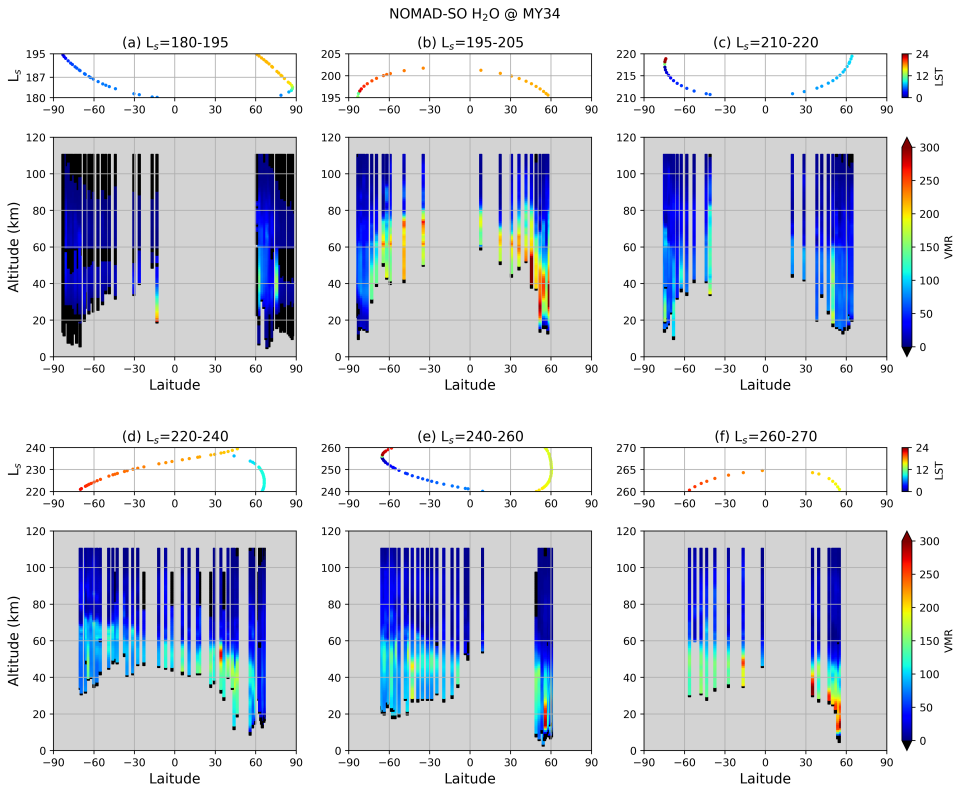

Figure 14. Latitudinal variation of the water vapor during the southern spring (northern autumn) of MY 34. Black regions are masked due to the low averaging kernels obtained during the retrievals.

50°N with the H_2O confined below 50-60 km, corresponding to the global expansion of the lower atmosphere and the transport northwards by the main equator-crossing Hadley cell (Steele et al., 2014; Barnes et al., 2017). Finally, panel 14f shows the period close to the southern summer, hence temperature in southern hemisphere is expected to increase. Here we observe the same structure as in panels 14d and 14e but presenting larger VMR values and showing overall a wetter atmosphere and revealing an increase in the water being released into the atmosphere. Figure 15 shows the latitudinal distribution of water vapor obtained with the Mars PCM at different L_s during the progress of the GDS and noticeably reproduces features observed by NOMAD, although abundances in the model are overestimated particularly during the early decay of the storm.

The results we find here are in line with the conclusions in Aoki et al. (2019, 2022) where an increase in the water vapor abundance in the middle atmosphere was observed at 60°N-60°S during the peak of the GDS. During the decay phase of the GDS Aoki et

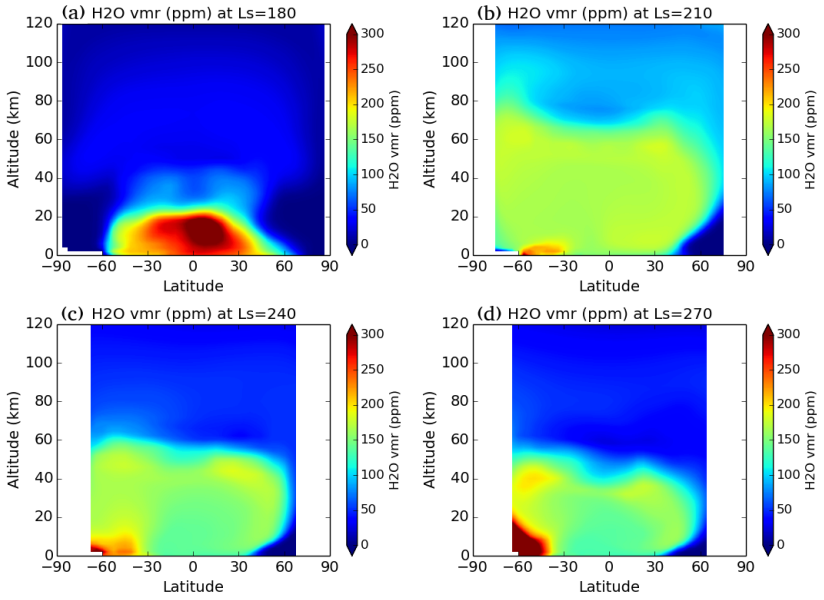

Figure 15. Latitudinal variation of the water vapor calculated with Mars PCM simulated for the evening terminator for MY 34 at L_s =180°, 210°, 240° and 270°.

al. (2019, 2022) found that the water vapor vapor in the middle atmosphere has peaks at latitudes greater than 60°S, which is also observed in this work.

4.1.4 Supersaturation and water ice

The saturation ratio expresses the ratio between the water vapor content present in the atmosphere ($\mu_{\mathrm{H_2O}}$), i.e. the retrieved H_2O VMR, over the saturated water vapor (μ_{sat}) as Equation 3 shows. To calculate the saturated H_2O VMR we use the expression Equation 4 for the saturation pressure over water ice (since in Mars water vapor condenses solely into ice) by (Murphy & Koop, 2005). The uncertainty associated to the saturation ratio (σ_S) showed in Equation 5 can be obtained through error propagation taking into account the uncertainties of the retrieved H_2O VMR ($\sigma_{\mu_{H_2O}}$) and temperature (σ_T).

$$S = \frac{\mu_{\mathrm{H_2O}}}{\mu_{\mathrm{sat}}} = \mu_{\mathrm{H_2O}} \frac{P_{\mathrm{tot}}}{P_{\mathrm{sat}}} \tag{3}$$

$$P_{\rm sat}(T) = \exp\left(9.550426 - \frac{5723.265}{T} + 3.53068 \cdot \ln(T) - 0.00728332T\right); \quad 110 < T < 273 \text{ K} \tag{4}$$

$$\sigma_S = \frac{P_{tot}}{P_{sat}}\sqrt{\sigma^2_{\mu_{H_2O}} + \mu^2_{H_2O}\left(\frac{5723.265}{T^2} + \frac{3.53068}{T} - 0.00728332\right)^2 \sigma^2_T} \tag{5}$$

In Figure 16(b-e) we present the first maps saturation ratio computed using the retrieved NOMAD SO temperatures for some occultations during MY34 when coincidences with orders 134-168 occur with order 149 (Lopez-Valverde et al., 2022). Although the number of processed occultations do not allow a detailed analysis, some structures can be identified. In the northern hemisphere, during the main activity of the GDS at $L_s \sim 200°$ we observe a clear region with supersaturation ($S > 10$) above 60 km up to 100 km. Later at $L_s \sim 230°$ a saturated layer appears at 80-100 km, decreasing in altitude to 60-80 km at $L_s \sim$ 240-260°. In the southern hemisphere, at $L_s \sim 220°$ we observe a clear supersaturated layer at 60-80 km that increases in altitude and thickness as the location of the observations decrease in latitude. The structures described above were also observed by Fedorova et al. (2020) with ACS data. A rough comparison with maps obtained with PCM temperatures (shown in Figure 16(c-f) can be done. Note that a detailed description of the PCM and NOMAD SO temperatures is presented in Lopez-Valverde et al. (2022). The main differences we observe appear in: (a) $L_s \sim 230°$ at 90 km and (b) $L_s =$ 250-260° at 70 km, both in the northern hemisphere. This supersaturation layers observed with the NOMAD temperatures, are not present in the map with PCM temperatures. This layers were also observed by (Fedorova et al., 2020) with ACS data and supports the temperature results from Lopez-Valverde et al. (2022). These features underline the necessity of using measured temperatures for these kind of studies. In future works we will extend the number of occultations with simultaneous H_2O and temperature observations in order to further investigate these and other features which may appear.

Also we analyze the coincidences between estimated supersaturation and water ice detections by Stolzenbach et al. (2022), where a detailed description and characterization of the nature of the Martian aerosols is presented. Here we use their results on the water ice. In this limited study analyzing the observations with collocated H_2O, temperature and aerosols measurements we have identified a total of 156 supersaturation events, in which

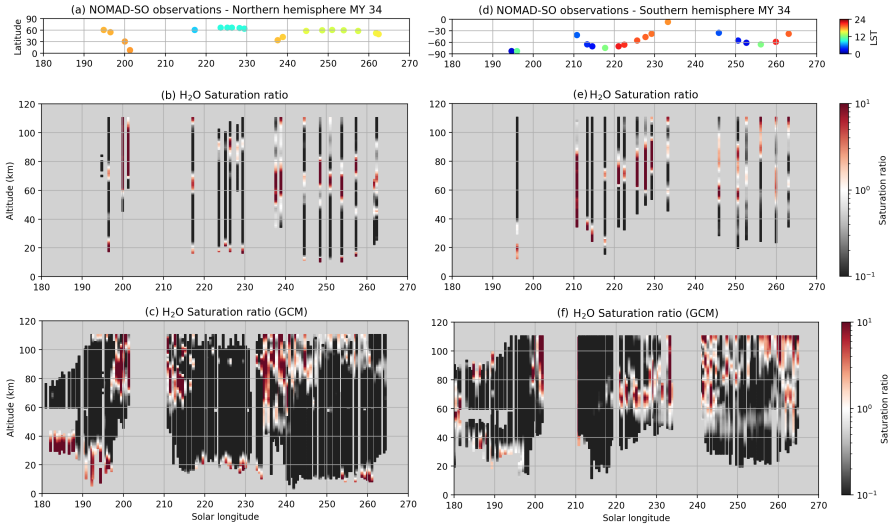

Figure 16. Saturation ratio calculated using retrieved NOMAD SO temperatures (middle panels) from Lopez-Valverde et al. (2022) for MY 34 at northern (b) and southern (e) hemispheres. Bottom panels show the saturation ratio obtained from the PCM temperatures for the northern (c) and southern (f) hemispheres. Top panels show the latitudes and the Local Solar Time of the observations analyzed for the northern (a) and southern (d) hemispheres.

about 16% of the events show an H_2O ice mass loading exceeding 10^{-13}g·cm^{-3}. Moreover, we find that most of the coincidences occur at the upper atmosphere between 50-90 km and more than 40% of the cases are confined at 70-80 km. In addition, we observe a few cases where supersaturation occurs towards the top of a cloud layer, as it is shown in the schematic model proposed by Poncin et al. (2022) for the saturation state of the atmosphere in the presence of cloud occurrence. The reduced number of the analyzed profiles for this study does not allow us to draw further conclusions. Four saturation ratio profiles are shown in Figure 17. Supersaturated layers can be observed at 80-100 km in panel (a) and at 70 km in panels (b) and (c), all of them coincident with H_2O ice detections and with atmospheric temperatures below the water vapor condensation limit. Panel (d) shows an example of a supersaturated layer at 70 km just above an ice cloud at 50 km. This finding with NOMAD SO observations suggests the presence of water ice clouds in a supersaturated atmosphere. Maltagliati et al. (2011) proposed the “scavenging" effect (falling ice cleaning the atmosphere from dust) as the main reason for the existence of supersaturated atmosphere, which would prevent the formation of water ice due to the absence of condensation nuclei. The water ice detected by Stolzenbach et al. (2022) and the coincidence with supersaturated layers found

598 in this work suggests that this mechanism is not the only reason for the supersaturation
599 on Mars and supports the results by Fedorova et al. (2020) found with ACS who also
600 observed supersaturation in presence of water ice. A specific study on supersaturation with
601 an extended dataset will be presented in future works.

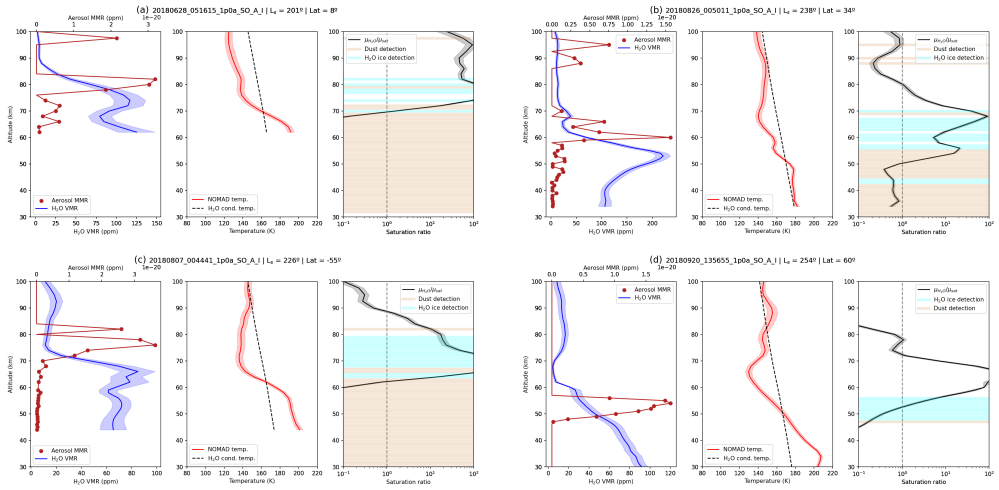

Figure 17. Profiles of water vapor, aerosols mass mixing ratio (MMR), temperature and water saturation ratio for four NOMAD SO observations. Left subpanel: Water vapor VMR (blue) and aerosol MMR (dark red). Center subpanel: NOMAD temperature (red) and water vapor condensation temperature (dashed). Right subpanel: Water saturation ratio (black), water ice detections (light blue) and dust detections (light brown). Vertical dashed line shows saturation ratio equal 1.

602 ## 4.2 Martian Year 35

603 ### *4.2.1 Seasonal variation*

604 As done in section 4.1, here we present seasonal variation maps the Figure 18 for the northern
605 (left panels) and southern (right panels) for MY 35 and an insight on the upper atmosphere
606 in Figure 19.

607 During this year, no global dust storm took place in the planet, so the usual seasonal
608 trend is expected to be observed. Compared with MY 34, in Figure 18 we observe noticeably
609 less water vapor in the atmosphere at the solar longitude range between $L_s = 190$-$230°$ in the
610 northern hemisphere. During this period, we observe a peak in the water vapor abundance
611 at $L_s \sim 205°$ in the southern hemisphere. This feature was also present during the same

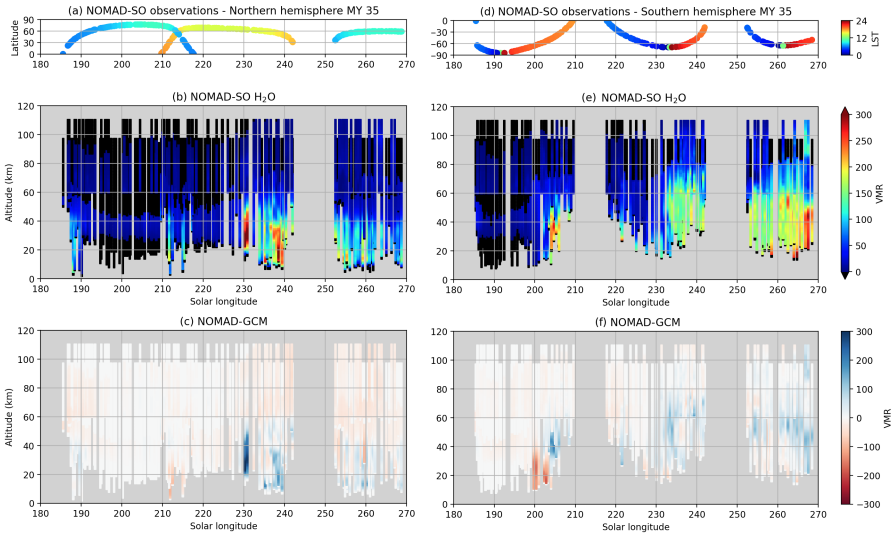

Figure 18. Seasonal vertical distribution maps of the retrieved water vapor (b,e) and the differences between the NOMAD SO retrievals and the PCM climatology (c,f) during the MY 35 in the Northern (left panels) and the Southern (right panels) hemispheres. Top panels (a,d) show the latitudes and the Local Solar Time of the observations analyzed. Black regions in panels (b) and (f) are masked due to the low averaging kernels obtained during the retrievals.

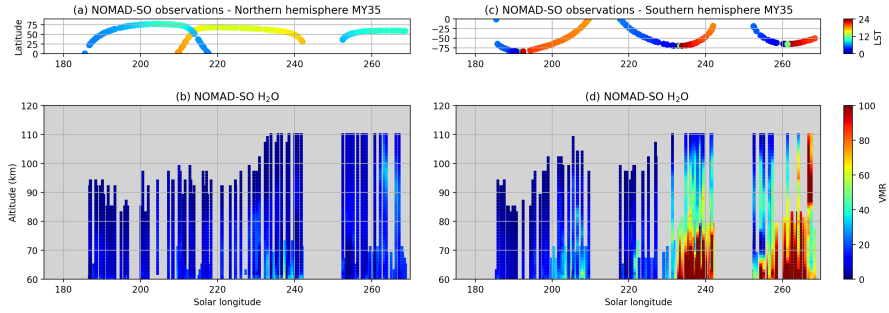

Figure 19. Seasonal vertical distribution maps of the retrieved water vapor at the upper atmosphere above 60 km during the MY 35 in the Northern (b) and the Southern (d) hemispheres. Top panels (a,c) show the latitudes and the Local Solar Time of the observations analyzed.

period in MY 34 but remarkably enhanced by the GDS. It is interesting to point out that the feature observed in the northern hemisphere also at this L_s is no longer present in MY 35. However, the reason of this absence is not only the non-GDS conditions during MY 35 but also the latitudinal coverage of the observations with measurements mostly at high latitudes (+75°N) near the northern polar cap. Similarly to what we observe during MY 34, as the southern spring progresses and southern summer kicks in, the water vapor present

in the southern hemisphere increases revealing high abundances in the period between L_s = 230-270° due to seasonal dust activity. Comparing the same period of these two Martian years, we notice larger abundances in the southern hemisphere during the last one, with water vapor reaching volume mixing ratios about 100 ppmv up to 80 km at at high latitudes during the perihelion, even reaching abundances >50 ppmv at 100 km at $L_s \sim 260°$ as shown in Figure 19, also reported by Belyaev et al. (2021). In contrast, northern hemisphere shows a similar seasonal trend in both Martian years, with the water vapor mostly confined below 50 km at mid latitudes.

4.2.2 Hygropause

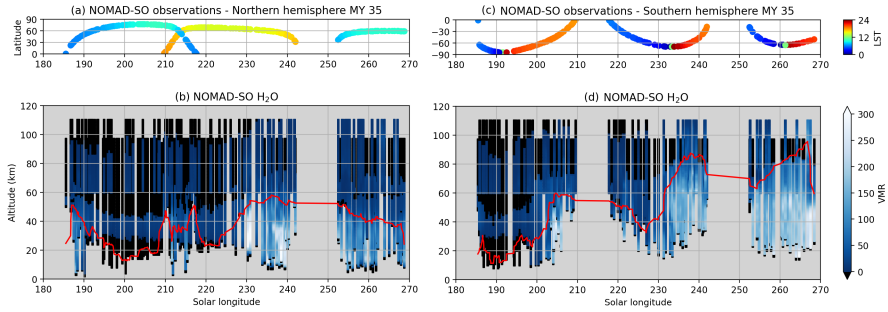

Figure 20. Seasonal vertical distribution maps of the retrieved water vapor (b,d) during the MY 35 in the Northern (left panels) and the Southern (right panels) hemispheres. The red line indicates the hygropause level. Top panels (a,c) show the latitudes and the Local Solar Time of the observations analyzed.

Figure 20 shows that the hygropause in the northern hemisphere is mostly confined below 30 km at high latitudes. However, at mid and low latitudes close to the equator, the hygropause level ascends up to 50-60 km. Compared to MY 34, during the period between L_s = 190-210°, the effects of the GDS are clearly visible, when hygropause near the equator reached an altitude about 80 km. The second part of the season is similar in both Martian years due to the similar dust conditions. In the southern hemisphere, looking at high latitudes we clearly observe how the hygropause increases in altitude as the spring progresses. With the water vapor mostly confined in the lower atmosphere at the beginning of the season, the hygropause level starts rising reaching an altitude of 80 km at the end of the spring. It is interesting to remark that in this year without a GDS, the topmost altitude we observe for the hygropause at L_s = 240-260° is 10 km higher than in the same period of MY 34,

638 although the temperature observed by ACS shows a similar trend in both MYs at this period
639 (Belyaev et al., 2021; Alday et al., 2021). Therefore, differences in the latitudinal sampling
640 could be a possible explanation of this feature (Aoki et al., 2022).

641 ### *4.2.3 Latitudinal variation*

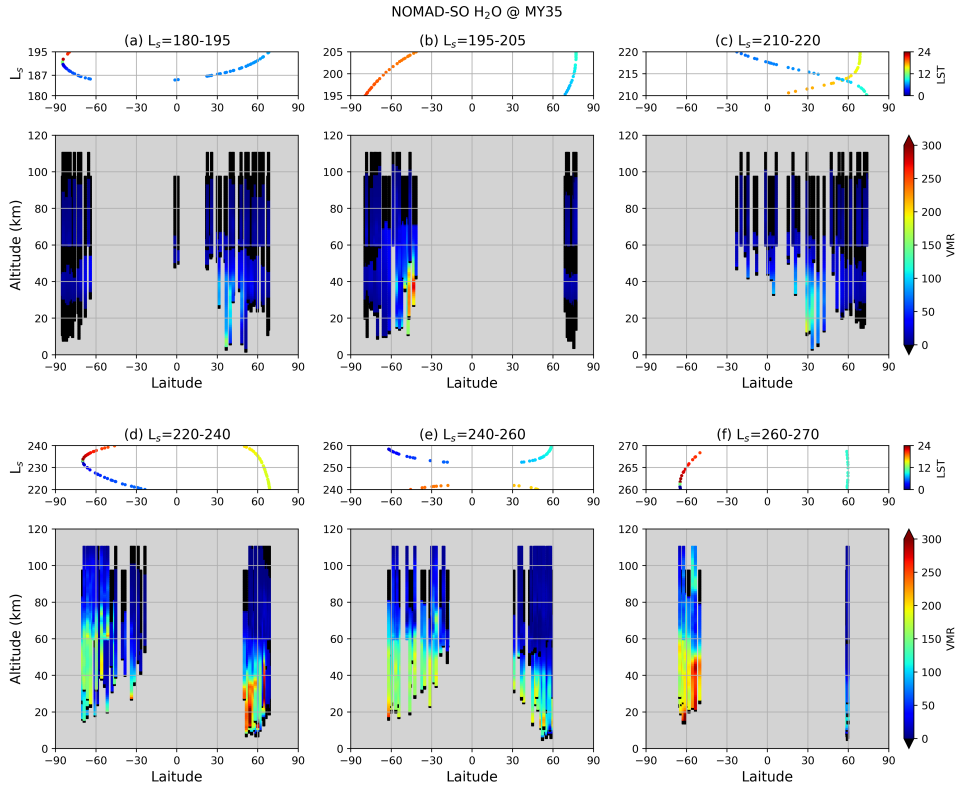

Figure 21. Latitudinal variation of the water vapor during the southern spring (northern autumn) of MY 35. Black regions in panels b and f are masked due to the low averaging kernels obtained during the retrievals.

642 In Figure 21 we show the latitudinal maps of the water vapor distribution during the ana-
643 lyzed period of MY 35, covering the same L_s ranges as in Figure 14 for a direct comparison
644 between both Martian years. Regardless of the poor coverage of the northern hemisphere,
645 panel 21b clearly show differences with the same panel in Figure 14 revealing that in this
646 period water vapor is mostly confined below 45 km and in latitudes lower than 50°S. This
647 observation agrees with the expected climatology according to the Mars PCM. Figure 22
648 shows the modeled latitudinal variation of the water vapor VMR by the PCM, and it proves
649 again the strong effects of the GDS with noticeable differences between panels 15b and 22b.

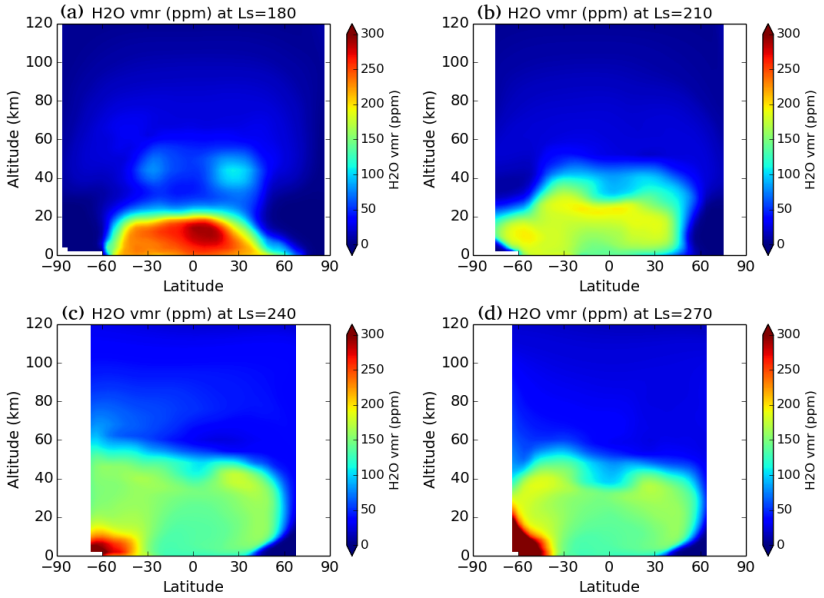

Figure 22. Latitudinal variation of the water vapor calculated with Mars PCM simulated for the evening terminator for MY 35 at L_s =180°, 210°, 240° and 270°.

As spring develops, we observe the expected seasonal trend in panels 21d-f, showing the same structure observed during in MY 34 due to the increase of the atmospheric temperature and the regular dust activity. Also, the observed water vapor in this period in both years agree with the expected climatology simulated by the PCM as shown in Figure 15.

5 Summary and conclusions

In this work we have presented the water vapor vertical distributions obtained for the first half of the perihelion season during Martian years 34 and 35, covering the Global Dust Storm (GDS) event of 2018 and hence characterizing the water vapor under GDS and non-GDS conditions. The direct comparison of the same season with different dust configurations during L_s ~180-210° allowed us to confirm the strong impact of a global dust event in the water distribution previously reported by MCS (Heavens et al., 2018b), ACS (Fedorova et al., 2020; Belyaev et al., 2021; Alday et al., 2021) and NOMAD (Aoki et al., 2019; Villanueva et al., 2021; Liuzzi et al., 2020) observations. The vertical profiles presented here have been obtained retrieving data from the NOMAD SO diffraction orders 134 and 168 and using the a priori density and temperature profiles from the Mars PCM (Forget et al., 1999; Lefèvre

et al., 2021), being the assumed profiles of minor importance for H_2O The main findings we report are as follows:

- During the strong activity of the GDS, we observe an intense peak in the water vapor showing abundances about 150 ppmv at 80 km in both hemisphere. After this short period, the abundance reduces to 50 ppmv in northern hemisphere and the high water vapor is only visible again at high southern latitudes. In contrast, during MY 35, water vapor does not exceed abundances of 50 ppmv above 50 km in the northern hemisphere.
- Due to the GDS peak, water vapor is mostly confined between 60°N and 75°S and revealing high abundances up to 80 km at mid and low latitudes close to the equator. This distribution is not observed during the same period of MY 35.
- At high southern latitudes we observe large water vapor abundances up to altitudes as high as 60 km, indicative of a warmer atmosphere during the period close to the southern summer solstice (L_s =220-270°). This feature is observed in both Martian years possibly due to similar dust conditions after the GDS.
- We report an estimation of the saturation ratio calculated using NOMAD SO temperatures, revealing multiple layers of supersaturation for MY 34. During the GDS, a clear region is observed above 60 km in both hemispheres where saturation ratio is greater than 10. Similar features are observed during the decay phase of the storm, revealing supersaturation layers above regions with high water vapor abundances in the middle atmosphere.
- We identify supersaturated layers in the presence of water ice, indicative of a condensation process going on at the terminator at the precise moment and local time of the NOMAD observations.
- The comparison of H_2O distributions derived from TGO SO data with other teams shows a qualitative agreement, although some discrepancies can be observed in the altitude range between 10-20 km, the origin of which needs to be further investigated in future works.

We plan to extend the dataset analyzed here to explore the later half of the perihelion season and further, to study the whole NOMAD SO dataset available to date. We also plan to revisit the saturation maps presented here but using NOMAD temperatures and also to extend and gain more insight into correlation between water ice and supersaturation.

Acknowledgments

The IAA/CSIC team acknowledges financial support from the State Agency for Research of the Spanish MCIU through the 'Center of Excellence Severo Ochoa' award for the Instituto de Astrofísica de Andalucía (SEV-2017-0709) and funding by grant PGC2018-101836-B-100 (MCIU/AEI/FEDER, EU) and PID2019-110689RB-I00/AEI/10.13039/501100011033 Grant PRE2019-088355 funded by MCIN/AEI/ 10.13039/501100011033 and by 'ESF Investing in your future'. F.G.G. is funded by the Spanish Ministerio de Ciencia, Innovación y Universidades, the Agencia Estatal de Investigación and EC FEDER funds under project RTI2018-100920-J-I00. ExoMars is a space mission of the European Space Agency (ESA) and Roscosmos. The NOMAD experiment is led by the Royal Belgian Institute for Space Aeronomy (IASB-BIRA), assisted by Co-PI teams from Spain (IAA-CSIC), Italy (INAF-IAPS), and the United Kingdom (Open University). This project acknowledges funding by the Belgian Science Policy Office (BELSPO), with the financial and contractual coordination by the ESA Prodex Office (PEA 4000103401, 4000121493) as well as by UK Space Agency through grants ST/V002295/1, ST/V005332/1 and ST/S00145X/1 and Italian Space Agency through grant 2018-2-HH.0. This work was supported by the Belgian Fonds de la Recherche Scientifique-FNRS under grant number 30442502 (ET-HOME). This project has received funding from the European Union's Horizon 2020 research and innovation program under grant agreement No 101004052 (RoadMap project). US investigators were supported by the National Aeronautics and Space Administration. We want to thank M. Vals, F. Momtmessin, F. Lefevre and the broad team supporting the continuous development of the LMD Mars PCM.

Open Research/Data availability

The NOMAD SO Level 1a calibrated data used in this work are available at the European Space Agency (ESA) planetaryarchive (`https://archives.esac.esa.int/psa`) and also at the NOMAD data center (`https://nomad.aeronomie.be/index.php/data` (Thomas et al., 2021; Vandaele et al., 2018)).

The results retrieved from the NOMAD SO measurements presented in this work are being archived and available at `https://doi.org/10.5281/zenodo.7085454` (Brines et al., 2022b)

References

Alday, J., Trokhimovskiy, A., Irwin, P. G., Wilson, C. F., Montmessin, F., Lefèvre, F., ... others (2021). Isotopic fractionation of water and its photolytic products in the atmosphere of mars. *Nature Astronomy*, *5*(9), 943–950.

Aoki, S., Vandaele, A., Daerden, F., Villanueva, G., Liuzzi, G., Thomas, I., ... others (2019). Water vapor vertical profiles on Mars in dust storms observed by TGO/NOMAD. *Journal of Geophysical Research: Planets*.

Aoki, S., Vandaele, A. C., Daerden, F., Villanueva, G. L., Liuzzi, G., Clancy, ... others (2022). Global vertical distribution of water vapor on Mars: Results from 3.5 years of ExoMars-TGO/NOMAD science operations.

Barnes, J. R., Haberle, R. M., Wilson, R. J., Lewis, S. R., Murphy, J. R., & Read, P. L. (2017). The Global Circulation. In R. M. Haberle, R. T. Clancy, F. Forget, M. D. Smith, & R. W. Zurek (Eds.), *Asteroids, comets, meteors - acm2017* (p. 202-228).

Belyaev, D. A., Fedorova, A. A., Trokhimovskiy, A., Alday, J., Montmessin, F., Korablev, O. I., ... Shakun, A. V. (2021). Revealing a high water abundance in the upper mesosphere of Mars with ACS onboard TGO. *Geophysical Research Letters*, *48*(10), e2021GL093411.

Brines, A., Lopez-Valverde, M., Funke, B., Ashimananda, M., Stolzenbach, A., Gonzalez-Galindo, F., et al. (2022a). Water vapor vertical distribution on mars during perihelion season of MY 34 and MY 35 with ExoMars-TGO/NOMAD observations.

Brines, A., Lopez-Valverde, M., Funke, B., Ashimananda, M., Stolzenbach, A., Gonzalez-Galindo, F., et al. (2022b). Water vapor vertical distribution on Mars during perihelion season of MY 34 and MY 35 with ExoMars-TGO/NOMAD observations [Dataset]. `https://doi.org/10.5281/zenodo.7085454`. doi: 10.5281/zenodo.7085454

Chaffin, M., Deighan, J., Schneider, N., & Stewart, A. (2017). Elevated atmospheric escape of atomic hydrogen from mars induced by high-altitude water. *Nature geoscience*, *10*(3), 174–178.

Chaffin, M., Kass, D., Aoki, S., Fedorova, A. A., Deighan, J., Connour, K., ... others (2021). Martian water loss to space enhanced by regional dust storms. *Nature Astronomy*, *5*(10), 1036–1042.

Fedorova, A. A., Bertaux, J.-L., Betsis, D., Montmessin, F., Korablev, O., Maltagliati, L., & Clarke, J. (2018). Water vapor in the middle atmosphere of Mars during the 2007

global dust storm. *Icarus*, *300*, 440–457.

Fedorova, A. A., Montmessin, F., Korablev, O., Luginin, M., Trokhimovskiy, A., Belyaev, D. A., ... others (2020). Stormy water on Mars: The distribution and saturation of atmospheric water during the dusty season. *Science*, *367*(6475), 297–300.

Forget, F., Hourdin, F., Fournier, R., Hourdin, C., Talagrand, O., Collins, M., ... Huot, J.-P. (1999). Improved general circulation models of the Martian atmosphere from the surface to above 80 km. *Journal of Geophysical Research: Planets*, *104*(E10), 24155–24175.

Gordon, I. E., Rothman, L. S., Hill, C., Kochanov, R. V., Tan, Y., Bernath, P. F., ... others (2017). The HITRAN2016 molecular spectroscopic database. *Journal of Quantitative Spectroscopy and Radiative Transfer*, *203*, 3–69.

Guzewich, S. D., Lemmon, M., Smith, C., Martínez, G., de Vicente-Retortillo, Á., Newman, C., ... others (2019). Mars science laboratory observations of the 2018/mars year 34 global dust storm. *Geophysical Research Letters*, *46*(1), 71–79.

Heavens, N. G., Kleinböhl, A., Chaffin, M. S., Halekas, J. S., Kass, D. M., Hayne, P. O., ... Schofield, J. T. (2018a). Hydrogen escape from Mars enhanced by deep convection in dust storms. *Nature astronomy*, *2*(2), 126–132.

Heavens, N. G., Kleinböhl, A., Chaffin, M. S., Halekas, J. S., Kass, D. M., Hayne, P. O., ... Schofield, J. T. (2018b). Hydrogen escape from Mars enhanced by deep convection in dust storms. *Nature Astronomy*, *2*(2), 126–132.

Holmes, J., Lewis, S., Patel, M., Chaffin, M., Cangi, E., Deighan, J., ... others (2021). Enhanced water loss from the martian atmosphere during a regional-scale dust storm and implications for long-term water loss. *Earth and Planetary Science Letters*, *571*, 117109.

Jiménez-Monferrer, S., López-Valverde, M. Á., Funke, B., González-Galindo, F., Piccialli, A., García-Comas, M., ... Bibring, J.-P. (2021). CO2 retrievals in the Mars daylight thermosphere from its 4.3 μm limb emission measured by OMEGA/MEx. *Icarus*, *353*, 113830.

Jurado Navarro, Á. A., et al. (2016). Retrieval of CO2 and collisional parameters from the MIPAS spectra in the earth atmosphere.

Kass, D., Schofield, J., Kleinböhl, A., McCleese, D., Heavens, N., Shirley, J., & Steele, L. (2020). Mars climate sounder observation of mars' 2018 global dust storm. *Geophysical Research Letters*, *47*(23), e2019GL083931.

Kley, D., Stone, E., Henderson, W., Drummond, J., Harrop, W., Schmeltekopf, A., ... Winkler, R. (1979). In situ measurements of the mixing ratio of water vapor in the stratosphere. *Journal of the Atmospheric Sciences*, *36*(12), 2513–2524.

Lefèvre, F., Trokhimovskiy, A., Fedorova, A., Baggio, L., Lacombe, G., Määttänen, A., ... others (2021). Relationship between the ozone and water vapor columns on mars as observed by spicam and calculated by a global climate model. *Journal of Geophysical Research: Planets*, *126*(4), e2021JE006838.

Liuzzi, G., Villanueva, G. L., Crismani, M. M., Smith, M. D., Mumma, M. J., Daerden, F., ... others (2020). Strong variability of Martian water ice clouds during dust storms revealed from ExoMars Trace Gas Orbiter/NOMAD. *Journal of Geophysical Research: Planets*, *125*(4), e2019JE006250.

Liuzzi, G., Villanueva, G. L., Mumma, M. J., Smith, M. D., Daerden, F., Ristic, B., ... others (2019). Methane on Mars: New insights into the sensitivity of CH4 with the NOMAD/ExoMars spectrometer through its first in-flight calibration. *Icarus*, *321*, 671–690.

Lopez-Valverde, M. A., Funke, B., Brines, A., Stolzenbach, A., Modak, A., Gonzalez-Galindo, F., et al. (2022). Martian atmospheric temperature and density profiles during the 1st year of NOMAD/TGO solar occultation measurements.

Maltagliati, L., Montmessin, F., Fedorova, A. A., Korablev, O., Forget, F., & Bertaux, J.-L. (2011). Evidence of water vapor in excess of saturation in the atmosphere of Mars. *science*, *333*(6051), 1868–1871.

Maltagliati, L., Montmessin, F., Korablev, O., Fedorova, A. A., Forget, F., Määttänen, A., ... Bertaux, J.-L. (2013). Annual survey of water vapor vertical distribution and water–aerosol coupling in the martian atmosphere observed by SPICAM/MEx solar occultations. *Icarus*, *223*(2), 942–962.

Modak, A., López-Valverde, M. A., Funke, B., Brines, A., Stolzenbach, A., Gonzalez-Galindo, F., et al. (2022). Retrieval of martian atmospheric co vertical profiles from the first year of NOMAD/TGO solar occultation observations.
(unpublished)

Montabone, L., Forget, F., Millour, E., Wilson, R., Lewis, S., Cantor, B., ... others (2015). Eight-year climatology of dust optical depth on Mars. *Icarus*, *251*, 65–95.

Montabone, L., Spiga, A., Kass, D. M., Kleinböhl, A., Forget, F., & Millour, E. (2020). Martian year 34 column dust climatology from mars climate sounder observations:

Reconstructed maps and model simulations. *Journal of Geophysical Research: Planets*, *125*(8), e2019JE006111.

Montmessin, F., Smith, M. D., Langevin, Y., Mellon, M. T., & Fedorova, A. A. (2017). The water cycle. *The atmosphere and climate of Mars*, *18*, 338.

Murphy, D. M., & Koop, T. (2005). Review of the vapour pressures of ice and supercooled water for atmospheric applications. *Quarterly Journal of the Royal Meteorological Society: A journal of the atmospheric sciences, applied meteorology and physical oceanography*, *131*(608), 1539–1565.

Navarro, T., Madeleine, J.-B., Forget, F., Spiga, A., Millour, E., Montmessin, F., & Määttänen, A. (2014). Global climate modeling of the Martian water cycle with improved microphysics and radiatively active water ice clouds. *Journal of Geophysical Research: Planets*, *119*(7), 1479–1495.

Neary, L., Daerden, F., Aoki, S., Whiteway, J., Clancy, R. T., Smith, M., ... others (2020). Explanation for the increase in high-altitude water on Mars observed by NOMAD during the 2018 global dust storm. *Geophysical Research Letters*, *47*(7), e2019GL084354.

Neefs, E., Vandaele, A. C., Drummond, R., Thomas, I. R., Berkenbosch, S., Clairquin, R., ... others (2015). Nomad spectrometer on the exomars trace gas orbiter mission: part 1—design, manufacturing and testing of the infrared channels. *Applied optics*, *54*(28), 8494–8520.

Olsen, K., Lefèvre, F., Montmessin, F., Fedorova, A., Trokhimovskiy, A., Baggio, L., ... others (2021). The vertical structure of co in the martian atmosphere from the exomars trace gas orbiter. *Nature Geoscience*, *14*(2), 67–71.

Olsen, K. S., Trokhimovskiy, A., Montabone, L., Fedorova, A. A., Luginin, M., Lefèvre, F., ... Shakun, A. (2021). Seasonal reappearance of hcl in the atmosphere of mars during the mars year 35 dusty season. *Astronomy & Astrophysics*, *647*, A161.

Poncin, L., Kleinböhl, A., Kass, D. M., Clancy, R. T., Aoki, S., & Vandaele, A. C. (2022). Water vapor saturation and ice cloud occurrence in the atmosphere of mars. *Planetary and Space Science*, *212*, 105390.

Smith, M. D. (2002). The annual cycle of water vapor on Mars as observed by the Thermal Emission Spectrometer. *Journal of Geophysical Research: Planets*, *107*(E11), 25–1.

Smith, M. D. (2004). Interannual variability in TES atmospheric observations of Mars during 1999–2003. *Icarus*, *167*(1), 148–165.

Smith, M. D., Bougher, S. W., Encrenaz, T., Forget, F., & Kleinböhl, A. (2017). Thermal structure and composition. *The atmosphere and climate of Mars*, *18*, 42.

Steele, L. J., Lewis, S. R., Patel, M. R., Montmessin, F., Forget, F., & Smith, M. D. (2014). The seasonal cycle of water vapour on mars from assimilation of thermal emission spectrometer data. *Icarus*, *237*, 97–115.

Stiller, G. P. (2000). The Karlsruhe Optimized and Precise Radiative transfer Algorithm (kopra). -.

Stolzenbach, A., Lopez-Valverde, M. A., Funke, B., Brines, A., Modak, A., Gonzalez-Galindo, F., et al. (2022). Martian atmospheric aerosols composition and distribution retrievals during the 1st martian year of NOMAD/TGO solar occultation measurements.
(unpublished)

Stone, S. W., Yelle, R. V., Benna, M., Lo, D. Y., Elrod, M. K., & Mahaffy, P. R. (2020). Hydrogen escape from Mars is driven by seasonal and dust storm transport of water. *Science*, *370*(6518), 824–831.

Thomas, I. R., Aoki, S., Trompet, L., Robert, S., Depiesse, C., Willame, Y., ... others (2021). Calibration of NOMAD on ESA's ExoMars Trace Gas Orbiter: Part 1–The Solar Occultation channel. *Planetary and Space Science*, 105411.

Trompet, L., Vandaele, A., Thomas, I., Aoki, S., Daerden, F., Erwin, J., ... Patel, M. R. (2022). Carbon dioxide retrievals from NOMAD-SO on ESA's ExoMars Trace Gas Orbiter and temperature profiles retrievals with the hydrostatic equilibrium equation. I. Description of the method. *Journal of Geophysical Research: Planets, submitted*.

Vandaele, A. C., Lopez-Moreno, J.-J., Patel, M. R., Bellucci, G., Daerden, F., Ristic, B., ... others (2018). NOMAD, an integrated suite of three spectrometers for the ExoMars trace gas mission: Technical description, science objectives and expected performance. *Space Science Reviews*, *214*(5), 1–47.

Vandaele, A. C., Neefs, E., Drummond, R., Thomas, I. R., Daerden, F., Lopez-Moreno, J.-J., ... others (2015). Science objectives and performances of NOMAD, a spectrometer suite for the ExoMars TGO mission. *Planetary and Space Science*, *119*, 233–249.

Villanueva, G. L., Liuzzi, G., Aoki, S. W., Shohei adn Stone, Brines, A., Thomas, I. R., Lopez-Valverde, M. A., ... others (2022). The deuterium isotopic ratio of water released from the Martian caps as measured with TGO/NOMAD.

Villanueva, G. L., Liuzzi, G., Crismani, M. M., Aoki, S., Vandaele, A. C., Daerden, F., ... others (2021). Water heavily fractionated as it ascends on Mars as revealed by ExoMars/NOMAD. *Science Advances*, *7*(7), eabc8843.

von Clarmann, T., Glatthor, N., Grabowski, U., Höpfner, M., Kellmann, S., Kiefer, M., ... others (2003). Retrieval of temperature and tangent altitude pointing from limb emission spectra recorded from space by the michelson interferometer for Passive Atmospheric Sounding (MIPAS). *Journal of Geophysical Research: Atmospheres*, *108*(D23).